Distance and Proper Motion Measurement of The Red Supergiant, PZ Cas, in Very Long Baseline Interferometry H_2O Maser Astrometry

A Ph.D. Dissertation Presented to
Department of Space and Astronomical Science,
Graduate School of Physical Science,
The Graduate University for Advanced Studies

by
Kozue Kusuno

July 30, 2014

Abstract

Understanding mechanisms generation and preservation of spiral structure of spiral galaxies is an important theme in galaxy dynamics. Density wave hypothesis has been considered to play a major role to form spiral arms in the Milky Way. One of predicts of the hypothesis is that young objects on the spiral arms should have peculiar motions no larger than 10 km s^{-1}, which align each other in the outer Galaxy. On the other hand, VLBI astrometric observations have recently detected randomly directed peculiar motions of 20–30 km s^{-1} in number of high-mass star-forming regions. This thesis study has been conducted to understand the origin of large peculiar motions on the spiral arms in the Milky Way. We performed VLBI H_2O maser monitoring observations of the red supergiant, PZ Cas, at twelve epochs from 2006 April to 2008 May using VLBI Exploration Radio Astrometry (VERA). We fitted maser motions by a simple model composed of a common annual parallax and linear motions of the individual masers. The parallax subtracted maser motions were well modeled by combination of a common stellar proper motion and a radial expansion motion of the circumstellar envelope. We obtained the annual parallax of 0.356 ± 0.026 mas and the stellar proper motion of $\mu_\alpha^* \cos\delta = -3.7 \pm 0.2$, and $\mu_\delta^* = -2.0 \pm 0.3$ mas yr^{-1} eastward and northward, respectively. The annual parallax corresponds to a trigonometric parallax of $2.81^{+0.22}_{-0.19}$ kpc. By re-scaling the luminosity of PZ Cas in any previous studies using our trigonometric parallax, we locate PZ Cas on a H-R diagram and found that it approaches towards a theoretically evolutionary track of an initial mass of $\sim 25\ M_\odot$. The sky position and the distance to PZ Cas are consistent with the OB association, Cas OB5, which is located in a molecular gas supershell. We derived the peculiar motion of PZ Cas of $U_s = 22.8 \pm 4.4$, $V_s = 7.1 \pm 2.2$, and $W_s = -5.7 \pm 4.0$ km s^{-1}. We discussed three possibilities to explain the peculiar motion. We firstly compared the peculiar motions of PZ Cas and Cas OB5 to examine a runaway star hypothesis. Because PZ Cas's peculiar motion is close to the median of the distribution of the Cas OB5 member stars, we concluded that PZ Cas has a typical motion of Cas OB5. On the contrary, this means that Cas OB5 has a large peculiar motion. We secondly compared the peculiar motions of Cas OB5 with Cas OB4. Because Cas OB5 is located at the western edge of an H_{II} supershell while the Cas OB4 is located at the eastern side, an expanding motion in those OB associations was expected to be observed, although the velocity dispersions of the OB associations are very large. The problem with this hypothesis is that there are not enough energy sources to form the supershell so far. The last possibility is epicyclic motion hypothesis in galaxy dynamics. Recent large

N-body hydrodynamical simulations have shown that non-stationary spiral arms can be formed in a disk galaxy without the density wave. According to the simulation results, young objects in the disk have a randomly large peculiar motions because of the epicyclic motions as large as what the VLBI astrometric observations have shown. At this moment, although we have no concrete evidence to conclude which hypotheses between the later two explain the origin of the peculiar motion of PZ Cas, the epicyclic motion hypothesis may be plausible because of the lack of the energy source to form the supershell.

Contents

List of Figures

List of Tables

Chapter 1

Introduction

1.1 Spiral Structure of the Milky Way

The Milky Way is one of important astronomical objects gathering more than 200 billion stars in the convex, which rotates with an independent rotational speed of $\sim$220 km s^{-1} (Kerr & Lynden-Bell 1986). The diameter of the Milky Way is about 30 kpc, and the total mass is about 10^{11} $M_{\odot}$. The Milky Way is thought to be a typical spiral galaxy which consists of a central bulge with a bar structure, and multiple spiral arms. The spiral structure of the Milky Way was first recognized by Georgelin & Georgelin (1976) who measured kinematic distances of Galactic H_{II} regions in the whole Milky Way. It is divided into three classes: disk bright stars with ionized hydrogen region born in spiral arms, brightest and dense bulge stars, and halo with globular clusters. In addition to the stellar objects, interstellar medium composed of gas and dust exist with the mass of 1/20 and 1/2000 in the total mass of the stellar object in the Milky Way, respectively. The interstellar medium is distributed in the thin disk extendedly similarly with the distribution of the stellar object. One of major subjects of spiral galaxies is how they maintain their spiral structures. It is a wellknown phenomenon that spiral galaxies have flat rotation curves in which the rotation velocity does not depend on the Galactocentric distance, so that the spiral galaxies show a differential rotation. If the spiral structure comes from the rotation of the materials, it cannot be maintained for longer than several rotation periods, because the closer the material is located to the center the shorter the one revolution. This leads to a so-called winding problem.

A "density wave theory" was proposed as a hypothesis to solve the winding problem by C. C. Lin and F. Shu in 1964. According to the hypothesis, the spiral structure is considered to be a result of propagation of a stationary density enhancement pattern (density wave) through a galactic disk with restorative forces stimulated by swing amplification (Toomre 1981, in Structure and Evolution of Normal Galaxies, ed. S. M. Fall & D. Lynden-Bell, 111-136). The interstellar medium orbiting in the disk is compressed

by a shock front when the density wave passes through. In a spiral galaxy, arms are composed of giant molecular clouds (GMCs) and more massive objects (giant molecular associations: GMAs), and young stars born in such clouds which are trailing the increased density of the materials. The density wave hypothesis predicts that there is a corotation radius at which an angular velocity of the density wave is equal to that of the galactic rotation. For example, it is considered that the density wave rotates at an angular velocity of roughly half of the galaxy rotation speed in the solar neighborhood. When the rotating materials pass the density wave, perturbation and shock are induced in the interstellar materials. Gases are compressed to increase the density to a factor of 5–8 higher than before in the vicinity of the spiral arms, and the maximum peaks of the density are often observed as dark lanes along the spiral arm. The gas compression along the spiral arms makes a trigger of gravitational instabilities to form stars. One of the characteristics of the density wave hypothesis in the galaxy dynamics is that young objects tend to deviate from the galactic rotation because a shear of the shock front induced by the density wave are formed in the spiral arms. We refer such an extra motion from the galactic rotation as to a "peculiar motion" or "non-circular motion". It is considered that the peculiar motions are not randomly directed but aligned well each other with a typical speed less than 10 km s^{-1}.

In terms of the Milky Way, the number of spiral arms and entrainment degree has not been understood well (Russeil 2003) because it cannot be possible to measure the Galactic objects in the disk accurately enough to discuss, especially for regions beyond the Galactic center.

1.2 Astrometry of Galactic Object

There are three methods to measure distances to Galactic objects. The first method is the photometric parallax for stellar clusters. From a Hertzsprung-Russell diagram (H-R diagram) of star cluster, the class, the spectral type, and the absolute magnitude of the stars is associated. In comparison with the spectra of the cluster observed accurately on the H-R diagram, we can calculate the absolute magnitude. Therefore, we evaluate a distance modulus of the main sequence as well as interstellar extinction. Because of a difficulty in evaluating the degree of the extinction, the photometric parallax has typically 20–30% uncertainty (Menten et al. 2007; Zhang et al. 2012b).

The second is the kinematic distance method, which has been used for estimating the distances to Galactic GMCs. By measuring radial velocities of the clouds, we can retrieve the distances with an assumption of the Galactic rotation curve. The measured distances by this method tend to be larger, sometimes by factors greater than 2, than the annual parallax (Reid et al. 2009b).

The last one is the annual parallax method to measure a tiny positional modulation caused by the Earth's orbital motion in a year. We are measuring the annual parallax of the sources with strong maser emission associated with high-mass star-forming regions (HMSFRs) and red supergiants, using Very Long Baseline Interferometry (VLBI) techniques. This method can determine source distances directly and geometrically without any assumptions of luminosity, extinction, metallicity, crowding, and so on. In addition, proper motions of sources can be obtained as well by monitoring the positional changes. *Hipparcos* project made great successes in measuring annual parallaxes of stars distances less than several hundred parsecs with an accuracy of 1 mas (Battrick 1989). Information of trigonometric parallaxes and proper motions together with radial velocities enable us to investigate three dimensional (3-D) motions of the stars in the Milky Way. VLBI astrometry is a very powerful tool to measure annual parallaxes of Galactic maser sources farther than sub-parsec distance: 52 maser sources have been measured using the Very Long Baseline Array (VLBA), VLBI Exploration of Radio Astronomy (VERA), and the European VLBI Network (EVN) (Reid et al. 2009b; Honma et al. 2012). A typical measurement accuracy of the distance of phase referencing VLBI observations is about 10 % (Ando et al. 2011; Asaki et al. 2010; Bartkiewicz et al. 2008).

1.3 Red Supergiant Stars

Red supergiants (RSGs) are evolved from massive OB stars ($10M_\odot \leq M \leq 50M_\odot$) after they leave a main-sequence in the H-R diagram (e.g. Massey 2003). They eventually become Wolf-Rayet stars phase and/or supernovae. RSGs are in He-burning phase of the massive stars. Their spectral types are K or M, and effective temperature is $3500-4500$ K (Massey 2003). Radii of massive stars increase to $300-2000$ $R_\odot$ in the RSG phase, and thus the luminosities reach 10^4–5×10^5 $L_\odot$. Although RSGs are very important to understand the last stage of the evolution of massive stars, it is observationally difficult to study RSGs because the number of massive stars is much smaller than that of low-mass stars in the Milky Way, and because the RSG phase is too short. For instance, the population of observed RSGs in the Milky Way is less than 100 among the total number of the stars of 200 billions, and very short duration of the RSG phase of typically $\sim 10^2$ yr makes it difficult to observe them. Circumstellar envelopes (CSEs) expanding outward from a central RSG as a stellar wind are often observed. Mass-loss rates of RSGs ranges 10^{-7}–10^{-4} $M_\odot$ yr^{-1}. Since envelopes often obscure the central stars, we have difficulties to obtain precise physical parameters of the central stars.

Bright masers are observed in CSEs of the RSGs at radio frequencies (e.g. Choi et al. 2008; Asaki et al. 2010). Because an intrinsic size of a maser source is typically 1 AU (Elitzur 1992), maser sources farther than a few kpc can be treated as point-like

sources in the VLBI observations. Using phase referencing VLBI techniques, we can measure tiny spatial motions of the masers which compose of internal motions because of CSE's expansion, annual parallaxes, and systemic proper motions of central stars. Precise annual parallax measurements provide us absolute magnitude of stars. In the RSG phase, a location in the H-R diagram is not strongly dependent on the effective temperature. By comparing the absolute magnitude with evolutionary tracks for various initial mass of massive stars, the initial mass of the star can be derived (Choi et al. 2008). Recent observational studies with the MERLIN suggest that H_2O masers around RSGs may be stable for longer than several years (Richards et al. 2012) while those masers of low- and intermediate-mass evolved stars can survive only for a few months. Therefore, the H_2O maser emissions of RSGs is considered to be a good probe to trace the CSEs in a long-term VLBI monitoring program.

RSGs are often observed in large star clusters in which more than several OB stars and RSGs are included. Such a star cluster is called an OB association whose typical size is $\sim$ 200 pc. OB associations are located around GMCs or H_{II} regions, and form parts of large-scale star-forming regions. The typical age of OB associations is about 10^6–10^7 yr, and the mass is about 10^3–10^4 $M_\odot$. Member stars of the OB associations were firstly catalogued by Humphreys (1978), and was later updated by Garmany & Stencel (1992).

Asaki et al. (2010) obtained the 3-D motion of another RSG, S Per, and found its systemic peculiar motion of 15 km s^{-1}. Considering the age of S Per being a few tens of million year, it is unlikely that the star shows a large peculiar motion which old stars often have. Asaki et al. (2010) pointed out that, since S Per is involved in the Per OB1 association, such a large peculiar motion of the RSG may be related to the whole motion of the Per OB1 association in the Milky Way. It is quite important to know whether RSGs' motions are aligned with their accompanying OB associations or not for further discussions about the Milky Way dynamics. In addition, RSGs can become distance indicators for OB associations by measuring the annual parallaxes very precisely with phase referencing VLBI. To determine trigonometric distance to OB associations is important for verification of the calibration method of the distance ladder.

1.4 Astronomical Masers

1.4.1 Maser Physics

Astronomical masers were firstly reported by Weaver et al. (1965) and Gundermann (1965) as intense OH radiations from several Galactic H_{II} regions in their 18 cm wavelength observations. Those intense radiations were explained by Perkins et al. (1966) and Litvak et al. (1966) using a theoretical idea of amplification caused by inverted populations be-

tween energy states of OH molecules. Intensive emission from materials with the inverted populations is referred to as Microwave Amplification by Stimulated Emission of Radiation (maser). In the regions radiating astronomical masers, the population on the energy states of maser molecules do not follow the Boltzmann distribution. The population of specific two energy states does not form the thermal equilibrium, so that the number of molecules at the higher energy state is larger than that at the lower state.

The population inversion is caused by enhanced excitation to a higher energy state by kinematical interactions in gas clouds (collisional pumping) or irradiation of strong infrared flux (radiative pumping). Let us introduce the standard radiative transfer equation,

$$\frac{dI_\nu}{dl} = -\kappa I_\nu + \epsilon \tag{1.1}$$

to develop a theoretical explanation of the maser emission. Here I_ν is a radiation intensity, l is a path length in the medium that the light is passing through, κ is a volume absorption coefficient, and ϵ is a volume emission coefficient. Here κ and ϵ is given by

$$\kappa = \frac{h\nu}{4\pi\Delta\nu}(n_1 - n_2)B, \tag{1.2}$$

$$\epsilon = \frac{h\nu}{4\pi\Delta\nu}n_2 A, \tag{1.3}$$

where n_1 and n_2 are a population densities of the lower and upper energy state of the molecules, A and B are a Einstein coefficients for spontaneous and stimulated emission respectively, h is Planck's constant ($= 6.63 \times 10^{-34}$ Js), ν is a center frequency of the line spectrum, $\Delta\nu$ is a Doppler line width. Assuming that κ and ϵ are constant in the medium, equation (1.1) is solved as follows:

$$I(l) = I(0)\exp(-\tau) + \frac{\kappa}{\epsilon}\{1 - \exp(-\tau)\}, \tag{1.4}$$

Here, the Rayleigh-Jeans approximation can be used in the microwave region as follows:

$$T_B = \frac{c^2}{2k_B\nu^2}I, \tag{1.5}$$

where T_B is brightness temperature, and k_B is Boltzmann's constant$= 1.38\times10^{-23}$ J K^{-1}. Then, we can express equation (1.4) using the brightness temperature:

$$T_B = [T_B(0) - T_{\rm x}]\exp(-\kappa l) + T_{\rm x}, \tag{1.6}$$

where $T_{\rm x}$ is excitation temperature for the transition. In the thermal equilibrium, $T_{\rm x}$ can be defined by

$$\frac{n_2}{n_1} = \exp\left(-\frac{h\nu}{k_B T_{\rm x}}\right). \tag{1.7}$$

If there are too many molecules in the upper energy state, we have the population inversion as $n_2 > n_1$ in equation (1.7). This leads to $\kappa < 0$ in equation (1.2). In this case, an optical depth (τ) takes a negative value, so that exponential amplification is caused rather than a decrease of the intensity as radiation travels along the pass. We have to note that the excitation temperature also becomes negative in the population inversion. Thus, as long as the population inversion persists, and as long as the region which contribute to maser photons with equally the radial velocity and the Doppler frequency continued, the maser emission is amplified.

Maser emission has been found from OH, H_2O, SiO, NH_3, and CH_3OH molecules. The astronomical maser emission has been observed from comets, molecular clouds in star-forming regions, CSEs of evolved stars, and active galactic nuclei. Very intensive masers are often observed in star-forming regions and evolved stars in the Milky Way. Therefore, the maser is one of the very important probes to study stars in the phases of their birth and death. The maser is also used to study scattering of the Galactic interstellar medium or to measure annual parallaxes of distant Galactic objects because angular size of the maser emitting region is very compact to be resolved as point source.

1.4.2 Stellar Masers

Stellar masers are often observed from red giant stars or red supergiant stars. Hereafter, we refer to those objects as evolved stars. Strong stellar masers are specially found from long period variable (LPV) stars with strong infrared excesses. These stars are surrounded by thick CSEs of gas and dust. Therefore, the stellar masers are related to the mass ejection from a central star.

Four molecules are known to emit astronomical masers from evolved stars in the radio wavelengths: SiO, H_2O, OH and HCN. Input energy to excite maser emission is 1800, 600, and 0 K for SiO ($v = 1$), H_2O, and OH molecules, respectively. SiO masers are excited at the vicinity of the central star ($R_* \sim 10^2 - 10^3$ $R_\odot$). The H_2O maser sources are located in the CSE just outside the SiO maser region ($\leq 10^4$ $R_\odot$), and the OH masers are located at the outermost part of the CSE ($> 10^5$ $R_\odot$).

We here describe the H_2O stellar masers in the evolved stars in more detail. Typical isotropic photon luminosities of LPV stars are about $\sim 10^4$ $L_\odot$, while RSGs emit around $\sim 10^5$ $L_\odot$. However infrared radiation from the central stars cannot excite the water molecules required for the observed water maser brightness. A velocity profile of the H_2O masers show time variation in a time scale from a few weeks to a few months. Although a time variation of stellar masers shows a good correlation with the stellar luminosity cycle, the H_2O maser maximum have a time phase lag of 0.1–0.2 period from the infrared and OH maser time variations (Engels et al. 1986). Therefore, the excitation mechanism of the stellar H_2O masers is considered to be the collision pumping (Deguchi 1977) rather

than the radiative pumping.

1.5 Astrometry with VLBI Phase Referencing Techniques

Several kinds of techniques have been developed for the VLBI astrometry to obtain accurate positions of compact radio sources. The most successful techniques is phase referencing, in which a target source is observed almost simultaneously with closely located reference sources. By subtracting fringe phases of a reference source from target fringe phases, a large amount of VLBI interferometer phase errors due to uncertainties in fluctuating atmosphere, frequency and clock standards, Earth orientation parameters, and baseline vectors between VLBI stations can be eliminated (Asaki et al. 2007). The first successful experiment of VLBI phase referencing was demonstrated by Bartel et al. (1986) for a pair of quasars, 3C345 and NRAO512. They showed that relativistic jet components of 3C345 are moving with subluminal speeds while the radio core is positionally very stable. Recently, Hada et al. (2011) investigated the radio core positions of M87 at the various frequencies with the VLBA using the phase referencing to determine the super massive black hole position. They observed the core of the AGN jet in several frequencies by using the phase referencing technique. They found that the central engine of M87 is located within 14–23 Schwarzschild radii of the radio core at 43 GHz.

Astrometry of Galactic maser sources is an important scientific target to study kinematics of the HMSFRs and evolved stars as well as the galaxy dynamics by measuring the positions of the stars in the sky with respect to a distant quasars as a positional reference. Xu et al. (2006) measured the distance to the W3(OH) HMSFRs in the Perseus arm using the VLBA. They observed for 8 hours on each of five epochs in 2003–2004. The distance to W3(OH) was successfully determined to be 1.95 ± 0.04 kpc. The photometric distance of W3(OH) is $\sim$2.2 kpc, so that they updated the distance with an accuracy of $\sim 2\%$. A number of astrometric observations with the H_2O masers at 22 GHz and methanol masers at 12 GHz have been carried out using the VLBA (Sanna et al. 2009; Reid et al. 2009a; Moscadelli et al. 2009; Xu et al. 2009; Zhang et al. 2009; Brunthaler et al. 2009). On the other hand, the VERA has observed the H_2O maser and SiO masers at 43 GHz towards HMSFRs and evolved stars (Asaki et al. 2014; Hirota et al. 2007; Choi et al. 2008; Sato et al. 2008).

1.6 Dissertation Goals

VLBI astrometry has revealed distances and 3-D motions of a number of Galactic maser sources in the last several years. Very precise astrometry with the VLBI techniques has just opened a new era for the Milky Way research with a typical accuracy of a few tens of micro arcseconds. Now we are able to pursue several spiral arms in the Milky Way with HMSFRs and RSGs close to the Sun (Reid & Honma 2013). The accumlation of the kinematic information of the Galactic objects will cover many research fields in astronomy and astrophysics including kinematic research of maser spots of star forming regions and stars, and in a quest of dynamical structure of the Milky Way to obtain fundamental parameters such as the distance from the Sun to the Galactic center, the rotation curve, and the solar motion.

On the other hand, we are also facing new questions in this research field. One of them now confusing us is large peculiar motions of HMSFRs. If the spiral structure of the Milky Way is formed by the propagation of the density wave, the young objects would not have large peculiar motions; the reality is that many of the sources have peculiar motions of 10–30 km s^{-1}. Although the origin of such large peculiar motions can be sometimes explained in line of super bubble due to supernova explosions (Sato et al. 2008) or cloud shuffling (Lee & Lim 2008), we cannot always find concrete reasons to cause such large peculiar motions.

To improve our understanding about the large peculiar motions in the Milky Way, we have investigated the 3-D motion of one of the RSGs, PZ Cas. In this study we selected this source with the following reasons:

(1) H_2O masers in the CSE of this star are stably observed for longer than a few years, the annual parallax and systemic proper motion of the central star can be estimated with high accuracy and reliability;

(2) The star is involved in a OB association, Cas OB5, which is considered to be located in the Perseus spiral arm (Humphreys 1978). Thus PZ Cas is probably located in the Perseus arm; and

(3) The star is as young as a few to a few tens of M yr so that the peculiar motion of this target has not been gravitationally affected by other Galactic objects.

PZ Cas and the member stars of Cas OB5 are located at the western edge of a H_I supershell (Fich 1986), hence we can investigate whether the expanding motion of the shell affect the peculiar motion(s) of the stars.

In this thesis, we aim to achieve the following subjects to tackle the most important science theme; to search for the origin of the large peculiar motions of young objects in the spiral arms.

(1) we make the H_2O maser image of PZ Cas for the first time.

(2) In order to track the maser emissions as long as possible, we improve the data reduction scheme to compensate the lack of the sensitivity.

(3) We measure the annual parallax and systemic proper motion of the central star very precisely to obtain the peculiar motion of the star.

(4) Using the obtained distance, the astrophysical parameters of PZ Cas such as the luminosity and the initial mass are updated.

(5) We investigate whether the peculiar motion of PZ Cas is comparable to those of the other Galactic sources in the Perseus spiral arm. If it is as large as those of the other sources, we pursuit the origin of the peculiar motion.

For the above purposes, we made use of the VERA archive data of PZ Cas monitoring program conducted from 2006 Apr to 2008 May, almost two years, with VLBI phase referencing technique. In Chapter 2, observation and data reduction of PZ Cas are described. Results of the monitor program are shown in Chapter 2 as well. We discuss the research results in Chapter 3. We summarize our conclusions in Chapter 4.

Chapter 2

VLBI Astrometry Observations of Red Supergiant

In Chapter 2, first we describe characteristics of the target source, PZ Cas, and its environment. Next we mention the VLBI phase referencing observations for the source using the VERA. Several aspects of the VLBI array are also described. We introduce a new phase correction method called Direct Phase Transfer in the part of the data reduction. Finally we figure out astrometric results for PZ Cas.

2.1 Observational Target and Environment

In this study, our main research target is VLBI astrometry for the red supergiant, PZ Cas. Spectrum type of PZ Cas varies in M2-M4Ia. According to General Catalogue of Variable Stars (GCVS), PZ Cas is a semiregular variable star with the period of 925 days. The minimum and maximum values of the magnitude is 11.6 and 12.9, respectively. The effective temperature of PZ Cas is calculated to be 3600 K (Levesque et al. 2005). Mass loss rate is computed to be 6.5×10^{-6} $M_{\odot}$ yr^{-1} (Mauron & Josselin 2011).

H_2O and OH masers have been detected in the spectrum profile of the star (Dickinson 1976; Dickinson & Chaisson 1973). On the other hand, SiO masers detection has not been reported yet. The H_2O maser profiles of PZ Cas show double peaks (Dickinson 1976). Later its profile was changed to a single peak spectrum (Shintani et al. 2008). Spatial distribution of the H_2O and OH masers around PZ Cas has not been imaged.

PZ Cas is catalogued as a member star of an OB assoaication, Cas OB5 (Humphreys 1978; Garmany & Stencel 1992). According to Garmany & Stencel (1992), the Cas OB5 association has 65 member stars including five RSGs as shown in Figure 2.1. *Hipparcos* (Perryman et al. 1997) has measured proper motions of 15 stars out of the 65 stars. The photometric parallax to Cas OB5 is reported to be 2.5 kpc (Humphreys 1978). Fich (1986) reported that there exists a large shell-like structure (supershell) to Cas OB5 with

the radius of 190 pc, the velocity of $\sim$ 20 km s^{-1}, and blown mass of $\sim$ 7.5 $\times$ 10^5 M$_\odot$.

2.2 VERA Observations of PZ Cas

The VERA is a Japanese VLBI array of National Astronomical Observatory of Japan (NAOJ) for conducting VLBI phase referencing astrometry observations. A conceptual illustration of the VERA is shown in Figure 2.2. The VERA has four antennas located at Mizusawa, Iriki, Ogasawara, and Ishigakijima (coded as MIZNAO20, IRIKI, OGASA20, and ISHIGAKI, respectively) with baseline range from 1000 km to 2300 km. Each radio telescope has 20m aperture size in diameter. The main project of the VERA is to explore the 3-D structure and dynamical of the Milky Way based on high-precision astrometry of Galactic maser sources. A significant feature of the VERA antennas is the dual-beam receiving system as shown in Figure 2.3 which allows us to simultaneously observe a target and reference source within 2°.2 (Honma et al. 2003). Main observing frequency bands of the VERA are K-band (22 GHz) and Q-band (43 GHz). Annual parallaxes of 17 Galactic water maser sources have been measured using the VERA at 22 GHz (Honma et al. 2012).

VERA of PZ Cas at 22.2 GHz have been conducted at 12 epochs over two years. The observing epochs are listed in Table 2.1. In our monitoring program, one beam (beam A) observed PZ Cas, and another (beam B) observed a closely located continuum source, J233921.1+601011 (hereafter, abbreviated as J2339+6010), one of the VERA 22 GHz calibrator survey sources (Petrov et al. 2007), 1.7° away, as a position reference. The observation duration was eight to ten hours. Each observation was divided into several sessions for the simultaneous tracking of PZ Cas and J2339+6010, each separated by short-term sessions of bright calibrators (3C 454.3 and J230043.0+165514) for 15 min in order to check the observing systems. We prepared one baseband channel (BBC) with a bandwidth of 16 MHz for PZ Cas and 14 BBCs with a total band width of 224 MHz for J2339+6010 in left-hand circular polarization. VLBI cross correlation was carried out with the Mitaka FX correlator at NAOJ, Mitaka, Japan, to produce VLBI fringe data with 512 spectral channels for PZ Cas for the central 8 MHz bandwidth, corresponding to a velocity spacing of 0.2107 km s^{-1} for the H_2O $J_{K_-K_+} = 6_{16} - 5_{23}$ maser line. A typical frequency allocation after the cross correlation is listed in Table 2.2.

2.3 Data reduction

To describe the phase referencing and imaging analysis process, we often refer results of a specific epoch observation (epoch F on Mar 22, 2007) because we started the data analysis with this epoch data. We analyzed the VLBI data using the standard NRAO data reduction software, Astronomical Image Processing Software (AIPS), version 31DEC10.

2.3.1 Initial calibrations

Initial calibration tasks were common for both PZ Cas and J2339+6010. First, the amplitude calibration was carried out by using the system noise temperatures ($T_{\rm sys}$) and gain calibration data. The measurements of $T_{\rm sys}$ often have abrupt time variations, as shown in Figure 2.4, especially when rain falls happened during the observation. We consider such rapid and abrupt time variations owing to an absorption effect of water puddles on the top of the VERA antenna feedome. We carried out a polynomial fitting of the raw $T_{\rm sys}$ data after removing such abrupt changes. At epoch H, since $T_{\rm sys}$ was not recorded for either beams A or B of ISHIGAKI station. Instead, $T_{\rm sys}$ of OGASA20 was used for ISHIGAKI, because the atmospheric environment (temperature and humidity) is similar to each other. Note that minor amplitude calibration errors at this stage can be corrected later, using self-calibration. The system noise temperatures for beams A and B were basically approximated to be identical, so that the time variation of the system noise temperature must be mainly attributed to the common atmosphere.

In the next step, two-bit sampling bias in the analogue-to-digital (A/D) conversion in VLBI signal processing were corrected. Earth-orientation-parameters (EOP) errors, ionospheric dispersive delays, and tropospheric delays were calibrated by applying precise delay tracking data calculated with an updated VLBI correlator model supplied by the NAOJ VLBI correlation center. The instrumental path differences between the two beams were corrected using the post-processing calibration data supplied by the correlation center (Honma et al. 2008). The phase tracking centers for PZ Cas and J2339+6010 of the updated correlator model were set to the positions given in Table 2.3 for all the observing epochs.

2.3.2 Direct Phase Transfer in Phase Referencing

After the initial calibration, an image of the reference source, J2339+6010, was synthesized by using the standard VLBI imaging method with the fringe-fitting and self-calibration. We carried out the above process twice to make the image of J2339+6010: the first process started with a single point source model, and the second with the reference source image which has been made in the previous process. After imaging, the phase referencing calibration solutions were directly calculated from the reference source fringe data. A block diagram of the phase referencing analysis using the DPT is shown in Figure 2.5. The calibrating phase, $\Phi_{\rm cal}(t)$, at time t was obtained from the following calculation with a vector average of all the spectral channels in all BBCs:

$$\begin{aligned}\exp[i\Phi_{\rm cal}(t)] &= \sum_{n=1}^{N}\sum_{m=1}^{M}\exp\{i[\Phi^{\rm r}_{\rm raw}(n,m,t) \\ &+ 2\pi[\nu^{\rm r}_n + (m-1)\Delta\nu - \nu^{\rm t}_0]\Delta\tau^{\rm r}_{\rm g}(t) \\ &- \Phi^{\rm r}_{\rm v}(U(t),V(t))]\},\end{aligned}$$

where $\Phi^{\rm r}_{\rm raw}$ is raw data fringe phase of the reference source, and $\Phi^{\rm r}_{\rm v}(U(t),V(t))$ is the visibility phase calculated from the CLEAN components of the reference source image for a baseline with $U(t)$ and $V(t)$. $N = 14$ is the BBC number, $M = 64$ is the spectral channel number in the single BBC, $\nu^{\rm t}_0$ is the RF frequency of the strongest H_2O maser emissions in beam A, $\nu^{\rm r}_n$ is the RF frequency at the lower band edge of the n-th BBC for the reference source as listed in Table 2.2, $\Delta\nu = 250$ kHz is the frequency spacing in the single BBC for the reference source, m is the integer number indicating the order of frequency channel in the single BBC, $\Delta\tau^{\rm r}_{\rm g}(t)$ is the third-order polynomial fitting result of the temporal variation of the group delay obtained from the preceded fringe-fitting for the reference source. We refer to the phase calibration solutions obtained with this method as Direct Phase Transfer (DPT) solutions. The DPT solutions were then smoothed by making a running mean with the averaging time of 16 s in order to reduce the thermal noise. The smoothed DPT solutions are shown in Figure 2.6 as well as the one obtained with an ordinary AIPS phase referencing analysis (AIPS CL table), whose block diagram is shown in Figure 2.7. Note that the imaging process of J2339+6010 is common both in the DPT method (Figure 2.5) and the ordinary AIPS phase referencing analysis (this figure). Those two results are basically consistent with each other. Note that, even when solutions cannot be obtained with the fringe-fitting or the following AIPS self-calibration because of the signal-to-noise ratios (S/N) below a cutoff value, the DPT solutions were created from the raw fringe data, as shown for OGASA20 station in Figure 2.8. The final astrometric result with the smoothed DPT solutions is consistent with that with the AIPS CL table at epoch F.

Amplitude gain adjustment was performed using a third-order polynomial fitting for the amplitude self-calibration solutions for J2339+6010. Since S/N of J2339+6010 is unexpectedly low at epoch G, we could not obtain good solutions for J2339+6010 in the fringe-fitting. We therefore obtained the group delay solutions from 3C 454.3 and set the amplitude gain to the unity for all the observing time. The DPT solutions were created from the J2339+6010 fringe data together with the group delay solutions determined with 3C 454.3. At epoch I, since IRIKI did not attend the observation, we used the remained three stations in the data reduction.

2.3.3 Image Synthesis of PZ Cas

The Doppler shift in PZ Cas spectra due to Earth's rotation and revolution was corrected after the phase referencing. The observed frequencies of the maser lines were converted to radial velocities with respect to LSR (Local standard of rest) using the rest frequency of 22.235080 GHz for the H_2O $6_{16} - 5_{23}$ transition. Since the cross power spectra within the received frequency region show a good flatness both in the phase and amplitude, the receiver complex gain characteristics was not calibrated in this analysis. We inspected the cross power spectra for all the baselines in order to select a velocity channel of the maser emission which would be unresolved and not have rapid amplitude variation. At this step, fast phase changes with a typical time scale of a few minutes to a few tens of minutes can be removed by the phase referencing, but slow time variations including a bias component as shown in Figure 2.9 cannot. The maser image was distorted because of the residual time variations of the fringe phase on a time scale of several hours, which might be caused by uncertainties in the updated VLBI correlator model. We conducted the fringe-fitting for the selected velocity channel with the solution interval of 20 min. We fitted the solutions to a third-order polynomial as shown in Figurer 2.9 and removed it from both of the fringe phases of PZ Cas and J2339+6010. This procedure can remove the residual fringe phase error from the PZ Cas data while it is transferred to the J2339+6010 data. As a result, this leads to an improvement of the PZ Cas image quality but in turn to a distortion of the J2339+6010 image. This distortion of the reference source causes an astrometric error in the relative position between the sources, as later discussed in Chapter 2.

2.3.4 Evaluation of Image Quality

Figure 2.9 also shows the fringe phase residuals obtained with the AIPS CL table. Although the fringe-fitting results with the AIPS CL table can be almost identifiable to those with the DPT solutions, it is later noted that the image peak flux density at $V_{\rm LSR} = -42.0$ km s^{-1} with the DPT solutions is 2 % lower than that with the AIPS CL table at epoch F. In addition, the image root-mean-square noise resulting from the DPT solutions is 5 % higher than that resulting from the AIPS CL table. We can also see that the residual phases resulting from the DPT solutions in the fifth and sixth observing sessions in Figure 2.9 have a larger deviation than those resulting from the AIPS CL table. Although the number of the calibrated visibilities after applying the DPT amplitude is larger than that with the AIPS CL table, especially in the last two sessions, the visibilities with lower S/N might degrade the final image quality. We have to admit that the AIPS CL table may lead to a slightly higher quality in the image synthesis because the fringe-fitting and self-calibration take off visibility with low S/N. The problem is that

there were some observations whose data shows unexpectedly low S/N for certain baselines. For such cases, it was hard to create AIPS CL table with the fringe-fitting and self-calibration. From the following three reasons, we used the DPT solutions instead of the AIPS CL table for all the observing epochs: (1) the DPT is useful even when the fringe-fitting fails because of the low S/N; (2) the final astrometric results between the two methods have little difference; and (3) it is preferable to use a unified anaysis scheme for obtaining scientific results from a data set with the same (U, V) distribution.

The DPT solutions and the long-term phase calibration data were applied to the remaining frequency channels to make image cubes for the LSR velocity range of -23.0 and -60.8 km s^{-1} with the step of 0.2107 km s^{-1}. Image-synthesis with 60 μas pixel for a region of 4096×4096 pixels, roughly a 246×246-square milliarcsecond (mas) region, was made by using IMAGR. To initially pick up maser emissions in the maps, we used the AIPS 2-D Gaussian component survey task, SAD, in each velocity channel map in order to survey emissions. We visually inspected the surveyed Gaussian components one by one. We stored the image pixels larger than 5-σ noise level for a visually confirmed maser emission. Hereafter we define a maser "spot" as an emission in a single velocity channel, and a maser "feature" as a group of spots observed in at least two consecutive velocity channels at a coincident or very closely located positions.

2.3.5 Accuracy of the Relative Position of PZ Cas

In the phase referencing astrometric analysis, positions of the PZ Cas maser spots were obtained with respect to that of the J2339+6010 image. The positional error includes the effect of a peak position shift due to uncertainties in the VLBI correlator model (atmospheric excess path lengths (EPLs), antenna positions, EOP, and so on) for the sources. Hereafter we refer a relative position error of a pair of point sources using the phase referencing due to uncertainties in a VLBI correlator model as an astrometric error.

We conducted Monte Carlo simulations of phase referencing observations for the pair of PZ Cas and J2339+6010 to estimate the astrometric error. For generating simulated phase referencing fringes, we used an improved version of a VLBI observation simulator, ARIS (Astronomical Radio Interferometer Simulator, Asaki et al. 2007), with new functions simulating station clocks (Rioja et al. 2012) and amplitude calibration errors. In the simulations, we assumed that flux densities of PZ Cas and J2339+6010 of equivalently 10 Jy and 0.2 Jy for 15.6 kHz and 224 MHz bandwidths, respectively, which were determined from our observations. The sources were assumed to be point sources. The observation schedule and observing system settings in the simulations such as the recording bandwidth and A/D quantization level were adopted from the actual VERA observations. A tropospheric zenith EPL error of 2 cm and other parameters were set as suggested for VERA observations (Honma et al. 2010). For simplification of the simulations, reference

source position errors were not considered. The simulation results from 200 trials are shown in Figure 2.10. They show that the 1-σ errors in the relative position are 72 and 33 μas in right ascension and declination, respectively. We used these standard deviations as the astrometric error in the following analysis.

At epoch I, IRIKI station geographically located at the center of the VERA could not attend the observation, so that the astrometric accuracy may become worse with the remaining three stations. We conducted another simulation series for the three-station case, and the resultant astrometric accuracy is 101 and 39 μas for right ascension and declination, respectively. We therefore use this astrometric accuracy at epoch I in the following analysis.

2.4 Results

Maser features of PZ Cas are spatially distributed over a region of 200 $\times$ 200 square mas. We identified 52 maser spots which are assembled into 16 maser features. Those maser features were arranged in 11 maser groups which are labeled from *a* to *k* as shown in Figure 2.11. The groups *a* to *e*, and *g*, *h*, *i* have radial velocity range between -51.9 and -40.5 km s^{-1}. The groups *f*, *j*, and *k* which have been detected at one epoch have -52.3, -39.3, and -37.6 km s^{-1}, respectively. The radial velocities of the identified maser spots are close to the stellar systemic velocity ($V_{\rm LSR} = -36.16 \pm 0.68$ km s^{-1}). Groups *a* and *b* located to the north and southeast of the spatial distribution, respectively, are bright and have complicated structures while the other groups (*c* to *k*) have a rather simple structure. For the following annual parallax analysis, we selected 16 maser spots among 52 using the following two criteria. (1) Maser spots are detected with the image S/N greater than or equal to 7. (2) The maser spot was detected at 8 epochs or more. All the selected maser spots belong to either group *a* or *b* by chance.

2.4.1 Annual parallax

In the first step of the annual parallax analysis we performed a Levenberg-Marquardt least-square model fitting of the maser motions with the same way as that described by Asaki et al. (2010) using the peak positions of the selected maser spots. We adopted the astrometric error as mentioned in Section 2.3 and a tentative value of a morphology uncertainty (a positional uncertainty due to maser morphology variation) of 50 μas in the fitting, equivalent to 0.1 AU by assuming the distance of 2 kpc to the source. Figures 2.12 and 2.13 show the images and the fitting results of all the selected maser spots. The stellar annual parallax, π^*, was determined with the combined fitting with the Levenberg-Marquardt least-square analysis for all the selected spots. The obtained stellar annual

parallax is 0.380±0.011 mas at this stage.

If we carefully look at Figure 2.13, the maser spots do not seem to be properly identified with the image peak positions because multiple maser spots are spatially blended. This is caused when the multiple maser spots whose size is typically 1 AU (Reid & Moran 1981) are closely located comparing with the synthesized beam size of $\sim$ 1 mas in this case, equivalent to 2.6 AU at the distance of PZ Cas. To identify an individual maser spot properly, especially for blended structures, we performed AIPS JMFIT for the two-dimensional (2-D) multiple Gaussian component fitting of the emissions. Here we refer to a maser spot which can be identified with the image peak position as an isolated maser spot, and to a maser spot which cannot be identified with a single peak position because of the insufficient spatial resolution as a blended component. If we can identify 2-D Gaussian components using JMFIT, instead of SAD which automatically searches multiple spots, in the brightness distribution, we refer to such spots as identified spots. Figure 2.14 provides an example of the annual parallax least-square fitting for a maser spot using either the image peak position or the 2-D Gaussian peak. Table 2.4 lists our combined fitting results using the image peak only for the isolated spots, only for the blended components, and for all those involved in the two groups. We also tried to make another combined fitting using the Gaussian peak only for the isolated spots, only for the blended but identified spots with JMFIT, and all of them, as listed in the second column in Table 2.4. The combined fitting results for the isolated spots show little difference between the cases of image peak and Gaussian peak. On the other hand, the fitting result for the blended spots with JMFIT peak positions is definitely changed from that with the image peak for the blended components and become closer to that obtained with the isolated spots. If a maser spot is recognized as an isolated spot, in other words, if a maser cloud is spatially resolved into multiple spots in the image, the image peak position can be treated as the maser position. Figure 2.15 shows histograms of the selected 16 annual parallaxes using the image peak and Gaussian peak positions. We fitted the histograms to Gaussian curves. In the case of the image peak positions (left panel), a 1-σ of the Gaussian curve is 0.046 mas. On the other hand, the 1-σ for the case of the Gaussian peak position (right panel) is 0.039 mas. Because it seems that the water maser emissions of PZ Cas cannot be fully resolved and because the dispersion of the annual parallaxes using the Gaussian peak position is smaller than that using the image peak position, we adopted the Gaussian peak positions in our least-square model fitting. The model fitting results obtained from the individual spots are listed in Table 2.5. From the combined fitting analysis by using all the selected maser spots, we obtained the stellar annual parallax of 0.356 $\pm$ 0.011 mas with assumptions of the above astrometric error and morphology uncertainty at this stage.

Although maser features around RSGs are good tracers for astrometric VLBI during

several years (Richards, Elitzur, and Yates 2011) the morphology of the maser spots observed with the high resolution VLBI is no longer negligible for the precise maser astrometry. This monitoring observations of PZ Cas have been conducted quite so often for two years that we can investigate the contribution of the morphology uncertainty to the maser astrometry. Figure 2.16 shows the position residuals of the selected 16 maser spots after removing the stellar annual parallax of 0.356 mas, proper motion, and initial position estimated for each of the spots. The standard deviation of the residuals are 93 and 110 μas for right ascension and declination, respectively. Assuming that those errors have statistical characteristics of a Gaussian distribution, the morphology uncertainty is 59 ($=\sqrt{93^2 - 72^2}$) and 105 ($=\sqrt{110^2 - 33^2}$) μas for right ascension and declination, respectively, where 72 and 33 μas are the astrometric errors discussed in subsection 2.3.3. It is unlikely that the morphology uncertainty has different values between right ascension and declination, so that we adopt 105 μas as the morphology uncertainty on the safer side. Based on the trigonometric parallax of 0.356 mas, 105 μas is 0.29 AU at PZ Cas. We conducted the combined fitting with all the maser spots whose positions were determined with JMFIT, and obtained π^* of 0.356 ± 0.011 mas at this stage.

Note that the above error of the annual parallax is a result by considering the random statistical errors from the image S/N and the randomly changing maser spot position as well as a common positional shift to all the maser spots at a specific epoch due to the astrometric error. Because the majority of the maser spots and features in the current parallax measurement are associated with the maser group *a*, the obtained stellar annual parallax could be affected by a time variation of the specific maser features at a certain level. Assuming that all the 13 maser spots belonging to group *a* have an identified systematic error, the annual parallax error can be evaluated to be $0.011 \times \sqrt{13} = 0.040$ mas. On the other hand, if we assume that maser spots belonging to a certain maser feature have a common systematic error but that some of them have their own time variations, the annual parallax error should be estimated to be somewhere ranging between 0.011 and 0.040 mas. To evaluate the contributions of such a systematic error, we carried out Monte Carlo simulations introduced by Asaki et al. (2010) for our astrometric analysis. First we prepared the imitated data set of the 16 maser spots with position changes added by considering the fixed stellar annual parallax and the maser proper motions. Secondly we added an artificial positional offset due to the image S/N, the astrometric accuracy, and the morphology uncertainty to each of the maser spot positions. The positional offset due to the image S/N was given to each of the maser spots at each epoch independently. The positional offset due to the astrometric error is common to all the maser spots at a specific epoch, but randomly different between the epochs. In this paper, we assumed that the positional offset due to the morphology uncertainty is common to all the maser spots belonging to a specific maser feature at a specific epoch, but randomly different

between the features and the epochs. We assume the standard deviation of the maser morphology uncertainty is 105 μas, equivalent to the intrinsic size of 0.29 AU. In a single simulation trial, we obtain the stellar annual parallax for the imitated data set. Thirdly we carried out 200 trials in order to obtain the standard deviation of the stellar annual parallax solutions. The resultant standard deviation is 0.026 mas which can be treated as the annual parallax error in our astrometric analysis. The resultant estimate of the stellar annual parallax is 0.356 $\pm$ 0.026 mas, corresponding to $2.81\ ^{+0.22}_{-0.19}$ kpc.

2.4.2 Stellar Position and Proper Motion

Similar to the cases seen in other RSGs (VY CMa, Choi et al. 2008; S Per, Asaki et al. 2010; VX Sgr, Kamohara et al. 2005, Chen et al. 2006; NML Cyg, Nagayama et al. 2008, Zhang et al. 2012b), the maser features around PZ Cas are widely distributed over a 200×200 square mas (corresponding to 562×562 square AU at a distance of 2.81 kpc) while the velocity of the features (–52 to –37 km s^{-1}) are distributed more closely to the stellar systemic velocity than those found in other RSGs are. It is likely that the detected maser groups are located at the tangential parts of the shell-like circumstellar envelope, whose three dimensional velocity has a small line-of-sight velocity. We determined the proper motions of all detected maser spots identified at least in two epochs. Table 2.6 lists maser spots whose proper motions and positions were calculated with the stellar annual parallax determined above. Using the proper motion data listed in Tables 2.5 and 2.6, we then conducted the least square fitting analysis to obtain the position of PZ Cas and the stellar proper motion based on the spherically expanding flow model (Imai et al. 2011). The obtained stellar proper motion in right ascension and declination, $\mu^*_\alpha \cos\delta$=–3.7 $\pm$ 0.2 mas yr^{-1} and μ^*_δ=–2.0 $\pm$ 0.3 mas yr^{-1}, respectively. The astrometric analysis result for PZ Cas is listed in Table 2.7. The proper motions of the detected maser spots are shown in Figure 2.17 together with the stellar position indicated by the cross mark.

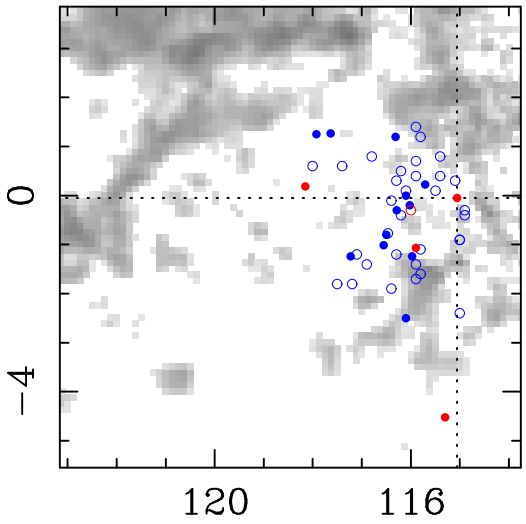

Figure 2.1: Cas OB5 member stars. The abscissa is the Galactic latitude, and the ordinate is the Galactic longitude. The blue and red circles represent OB stars and RSGs, respectively. The blue and red filled circles represent the member stars listed in the *Hipparcos* catalogue. The background grey scale is the CO (J=1–0) map reported by Dame et al. (2001).

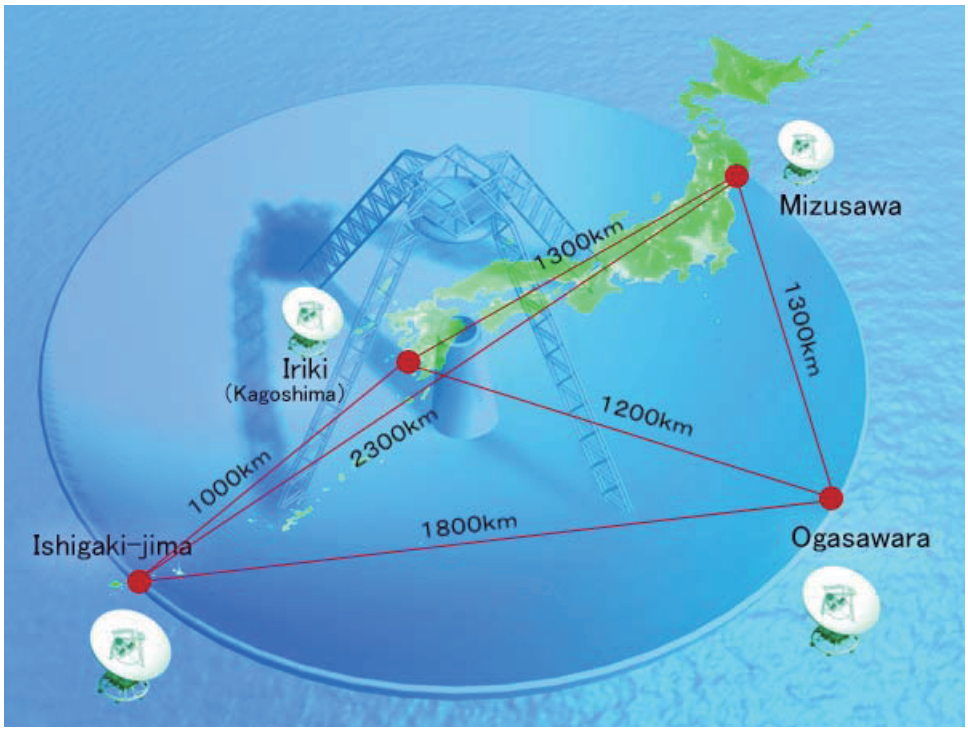

Figure 2.2: Conceptual illustration of the VERA. The VERA consists of four stations located at Mizusawa, Iriki,Ogasawara, and Ishigakijima. The maximum baseline is about 2300 km between Mizusawa and Ishigakijima. Each station has a radio telescope of 20 m diameter.

Figure 2.3: Steward-mount dual-beam platform of the VERA antennas.

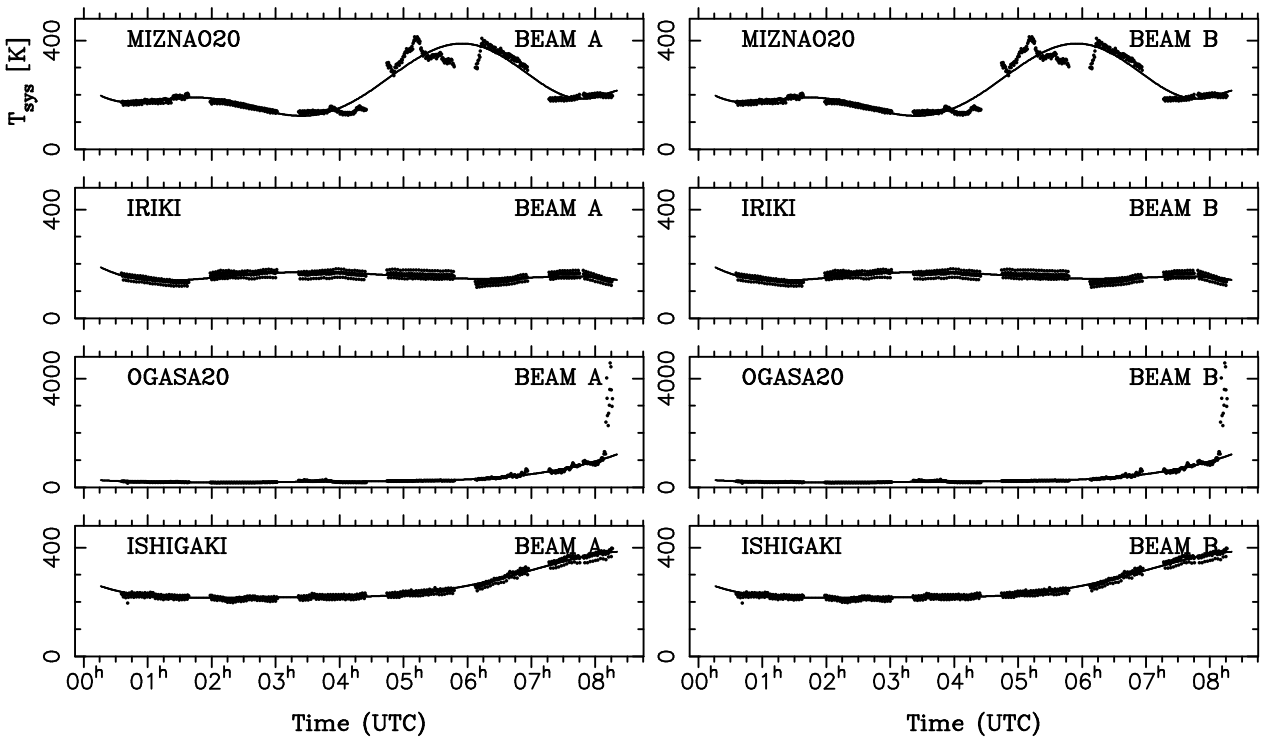

Figure 2.4: Time variation of system noise temperature at epoch F. The abscissa is time in UTC, and the ordinate is the system noise temperature in Kelvin. Dotted points are measurements, and the solid lines are the polynomial fitting curves after removing the abrupt changes. Left and right panels show beams A and B, respectively. From the top to bottom plot: MIZNAO20, IRIKI, OGASA20, and ISHIGAKI stations.

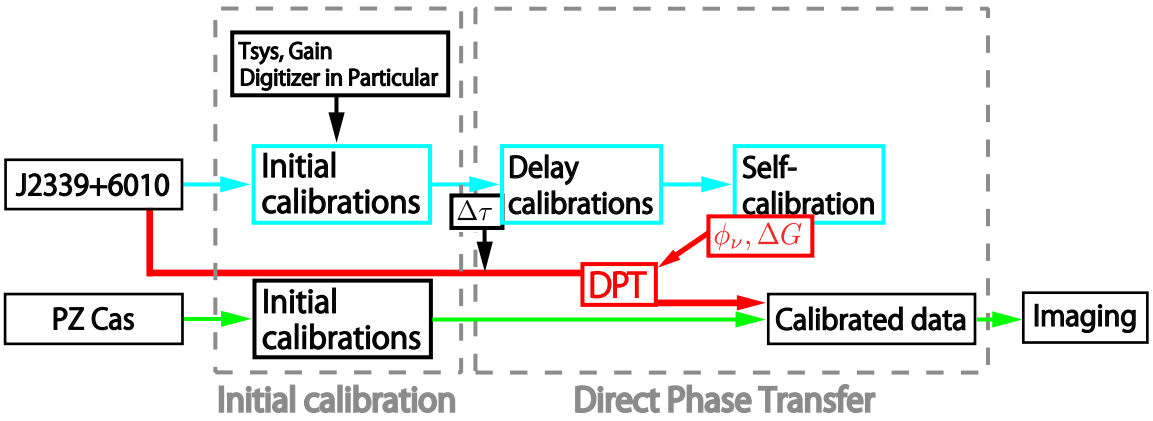

Figure 2.5: Block diagram of the Direct Phase Transfer (DPT) method for phase referencing VERA maser astrometry. The visibility phase, ϕ_ν, because of the structure of the J2339+6010 image is subtracted based on the CLEAN components obtained in the imaging process as shown with the blue arrows.

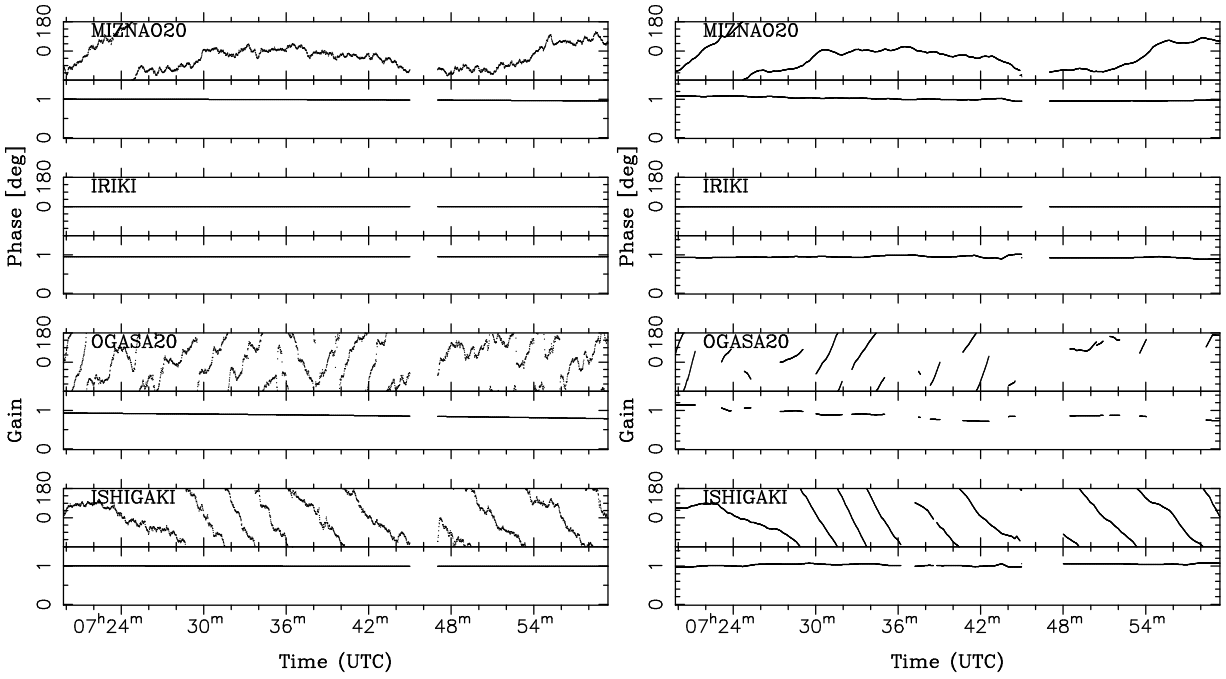

Figure 2.6: Complex gain calibration solutions obtained from J2339+6010 at epoch F for the phase referencing. IRIKI is the reference antenna. Each antenna has two plots: the abscissa is time in UTC, and the ordinate is the phase calibration data in degree and the amplitude gain for the upper and lower plot, respectively. The left and right plots show the direct phase-transfer (DPT) solutions introduced in Chapter 2, and those obtained in an AIPS phase referencing analysis (AIPS CL table), respectively. For making the AIPS CL table, the solution intervals are set to two, two and ten minutes for the fringe-fitting, phase-only self-calibration, and amplitude-and-phase self-calibration, respectively. From the top to bottom plot: MIZNAO20, IRIKI, OGASA20, and ISHIGAKI.

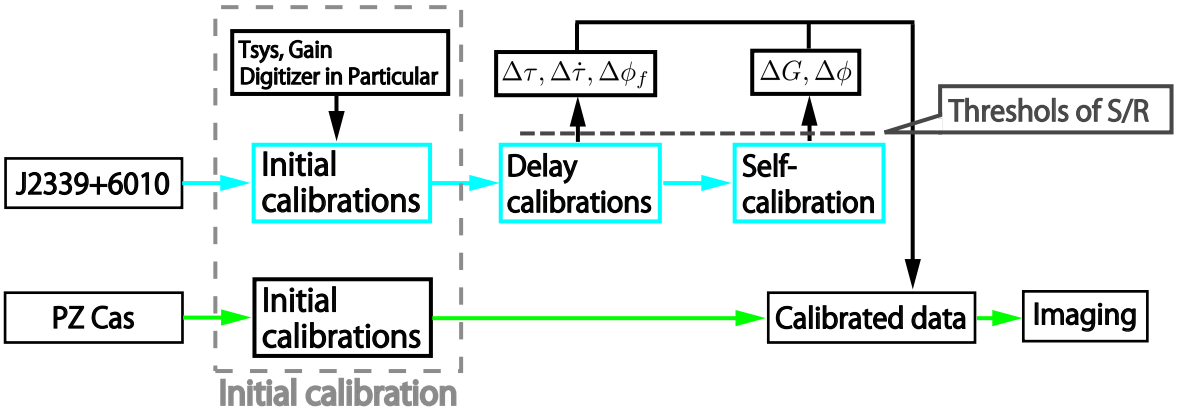

Figure 2.7: Block diagram of the ordinary AIPS phase referencing analysis to generate an AIPS CL table. In this thesis study, we adopted the S/N threshold of 6 to obtain complex gain solutions in the fringe-fitting and self-calibration.

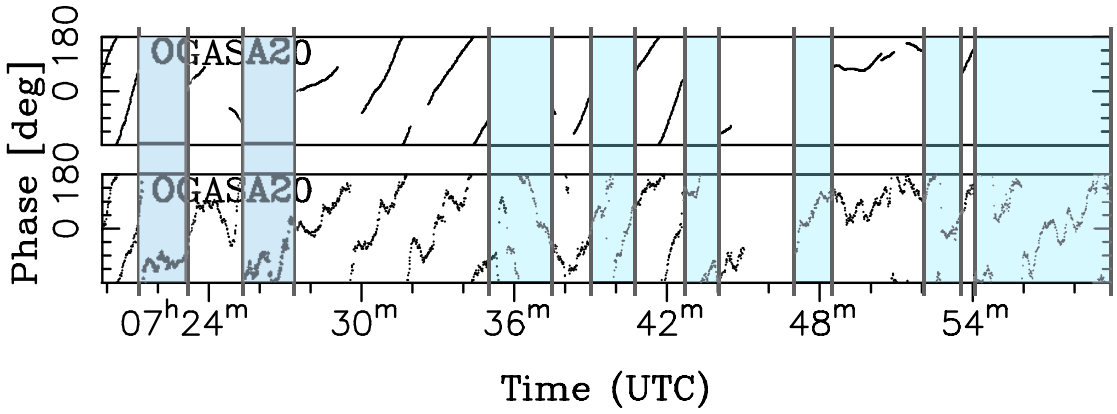

Figure 2.8: Phase calibration data as shown in Figure 2.5, but only for OGASA20. The top plot shows AIPS CL table with the ordinary AIPS phase referencing analysis. The bottom plot shows the DPT data. Light blue area is missing phase data by the AIPS phase referencing analysis.

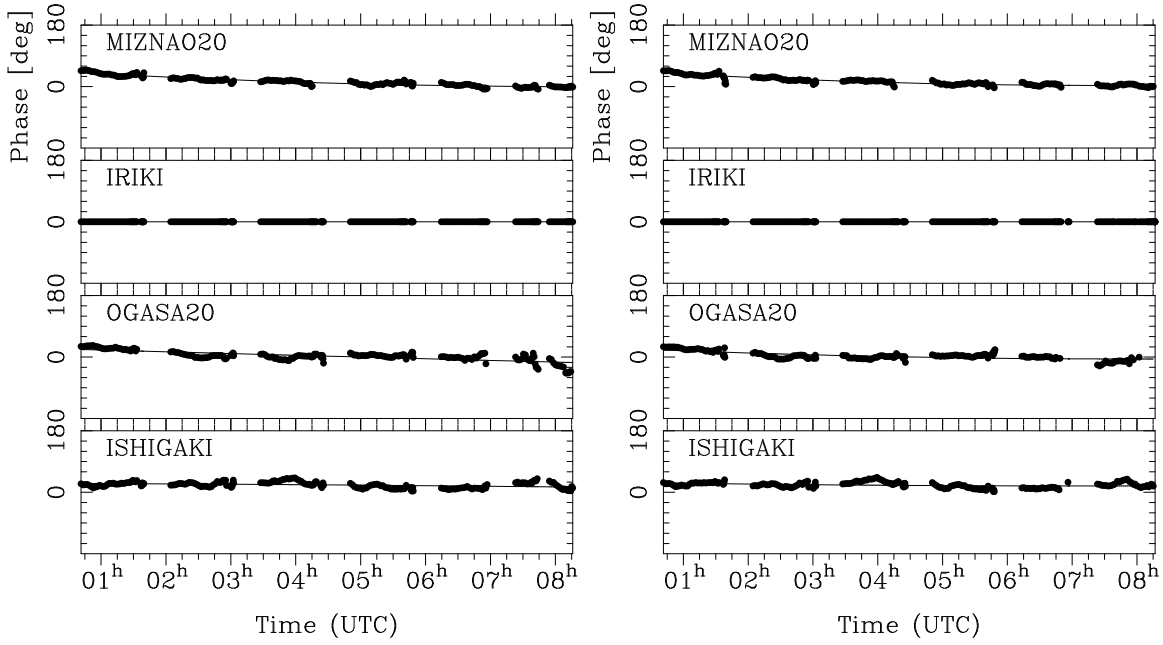

Figure 2.9: Phase solutions using the fringe-fitting with the solution interval of 20 min for the PZ Cas's brightest velocity channel ($V_{\rm LSR} = -42.0$ km s^{-1}) at epoch F. The abscissa is the time in UTC, and the ordinate is the phase in degree. IRIKI is the reference antenna. The dotted points are the fringe-fitting solutions, and the solid lines represent fitting results with a third-order polynomial for each station. Left and right plots show the fringe-fitting results after the phase referencing with the direct phase transfer calibration and the AIPS CL table, respectively. From the top to bottom plot: MIZNAO20, IRIKI, OGASA20, and ISHIGAKI.

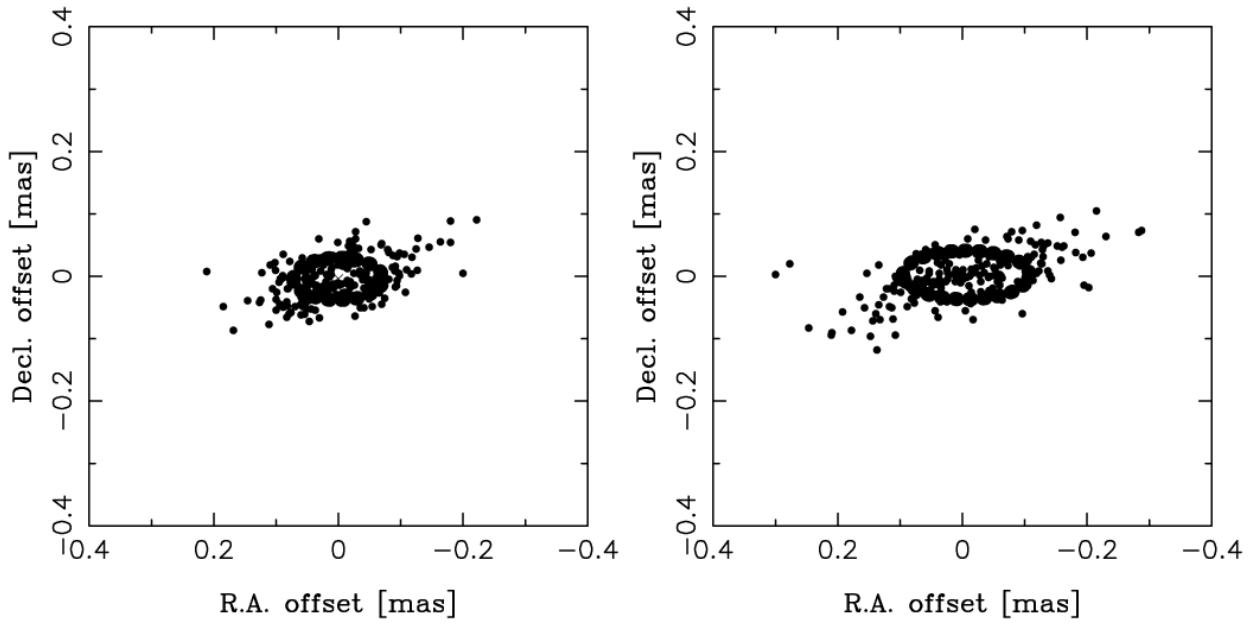

Figure 2.10: Astrometric observation simulation results for the pair of PZ Cas and J2339+6010. The dots represent PZ Cas's image peak positions relative to J2339+6010 at 22 GHz with the VERA for 200 trials. The ellipses represent 1-σ for the distributions. Left: the VERA full array case. Right: the VERA three-station case (MIZNAO20, OGASA20, and ISHIGAKI).

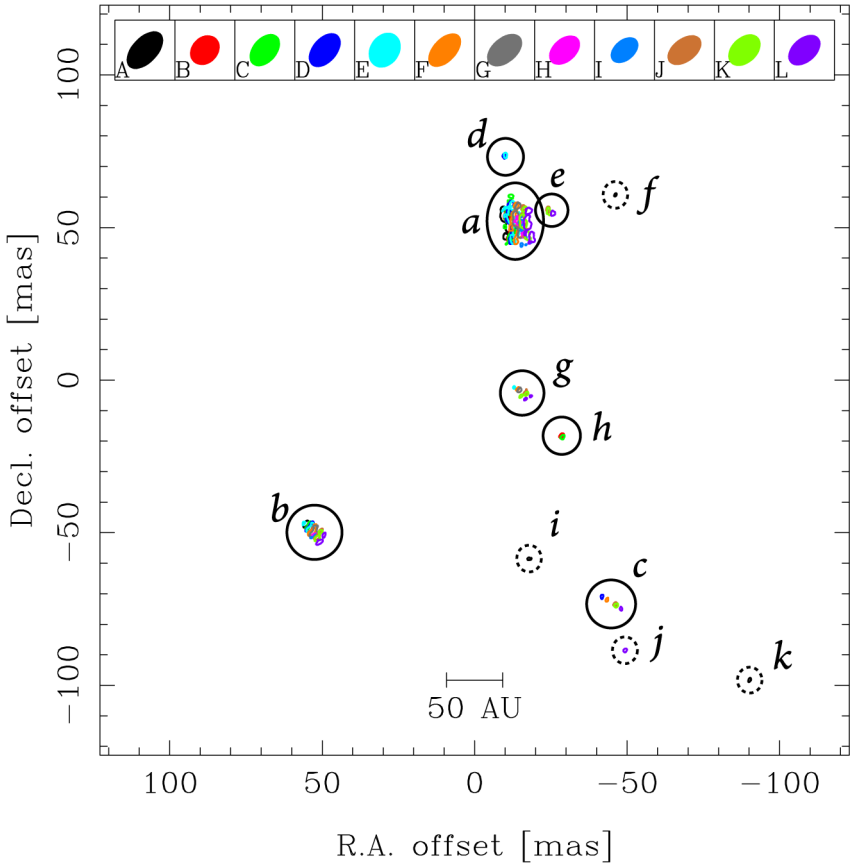

Figure 2.11: Spatial distribution of the PZ Cas H_2O masers in the 12 epochs. The outlines of maser features represent a 5-σ noise-level contour (418, 722, 661, 367, 467, 344, 309, 658, 686, 440, 313, and 285 mJy at epoch A, B, C, D, E, F, G, H, I, J, K and L, respectively). The synthesized beams are shown in the upper 1×1-square mas boxes. Maser features srrounded with circles represent maser groups. Groups f, i, j, and k are features detected at a single epoch. Group a is composed of four features, Groups b and g are composed of two features. The map origin is the phase-tracking center.

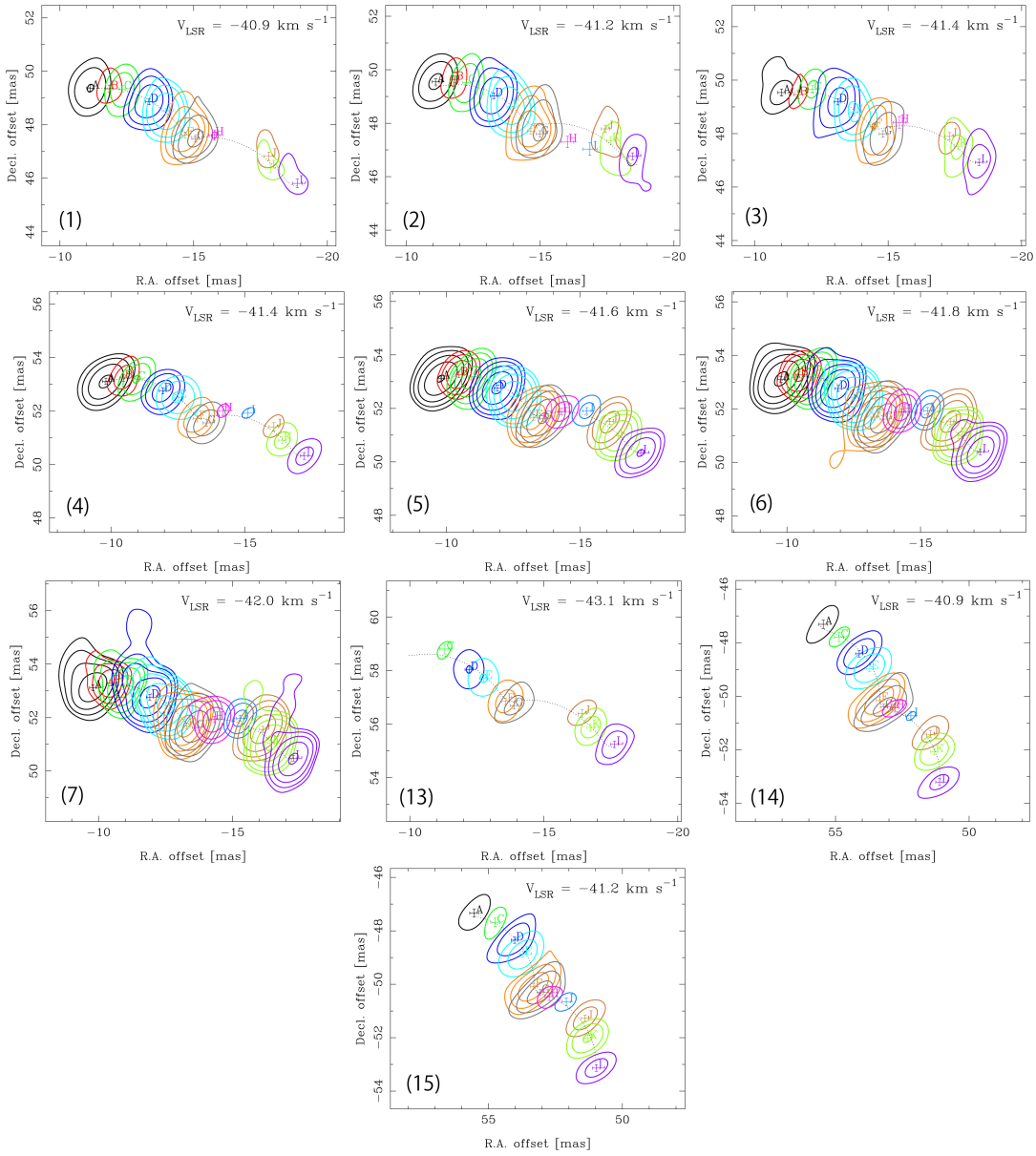

Figure 2.12: Spatial motions of 10 isolated maser spots. Color represents an observation epoch as shown in Figure 2.11. Dotted lines represent the best fit annual parallax and proper motion. The outermost contours show a 5-σ noise level, and contours are increased by a factor of power of 2. The number at the left bottom corner in each of the panels is the maser spot ID as listed in Table 2.5. Positional errors are displayed at the image peak positions. Dashed lines represent the least-squar fitting results of the spatial motion of an annual parallax and a linear motion for the maser peak positions.

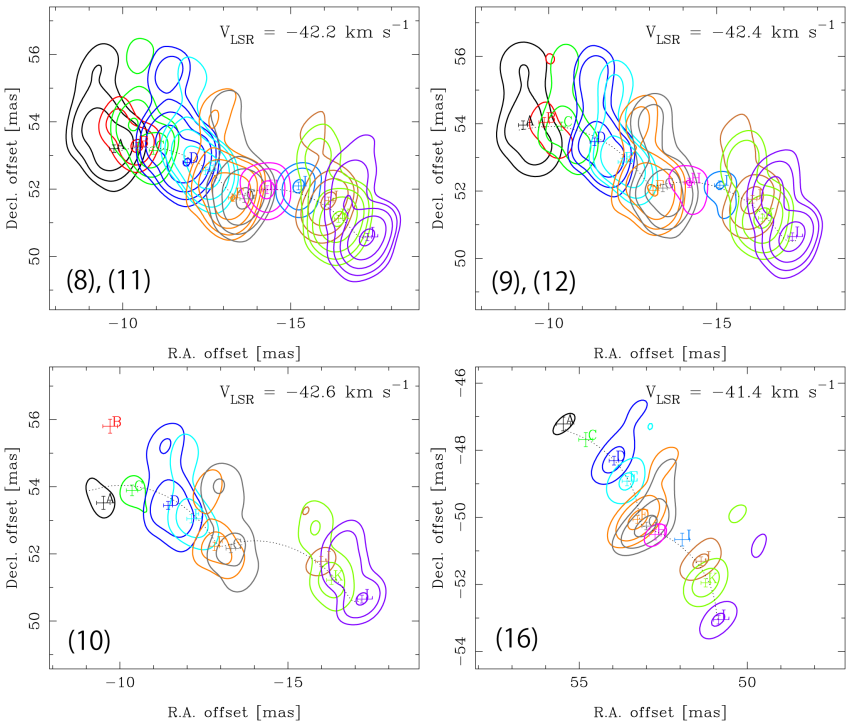

Figure 2.13: Same as Figure 2.12 but the maser spots identified as the blended component. The maser components in the upper two panels have two maser spots while the ones in the lower panels have a single spot.

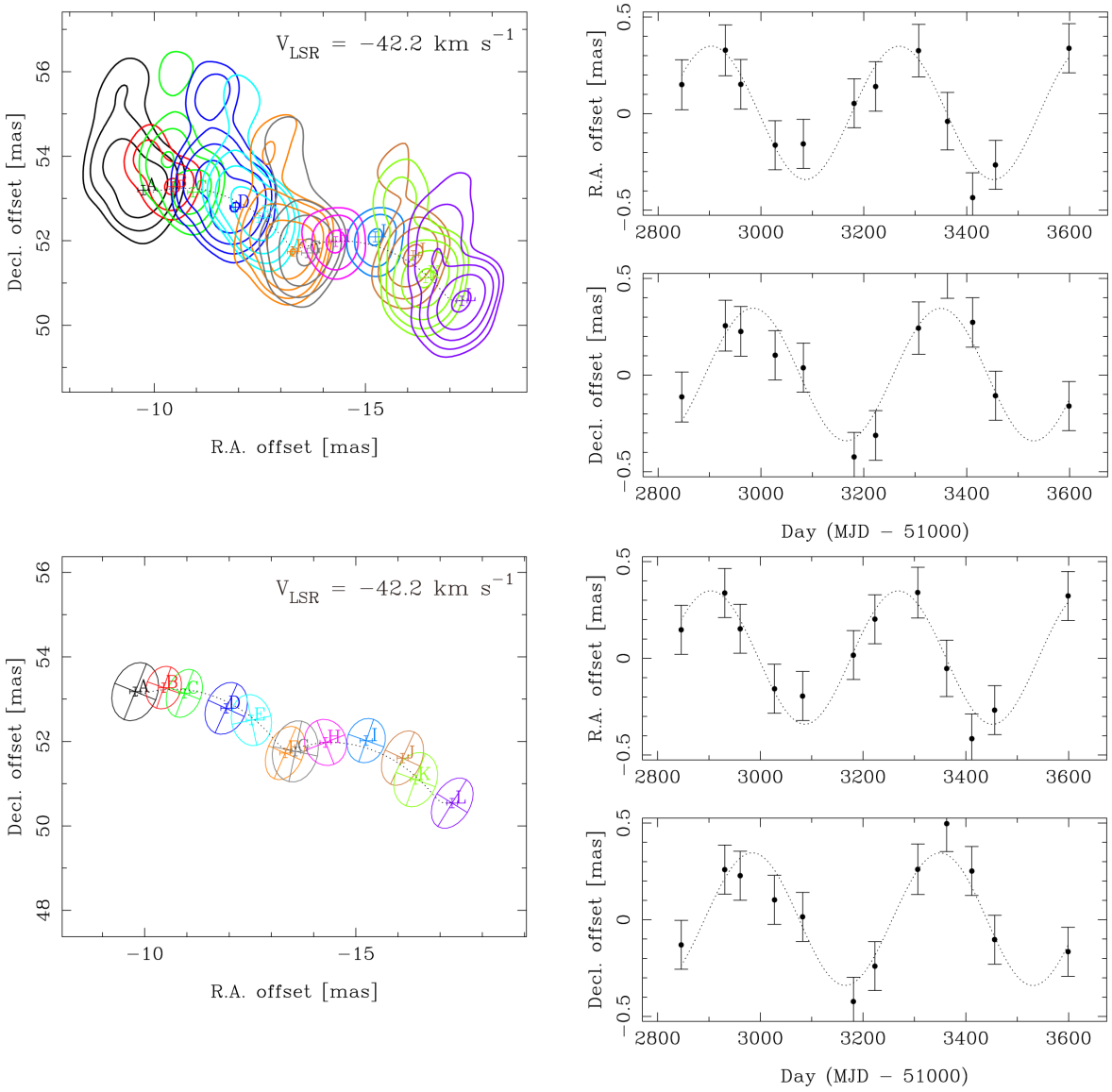

Figure 2.14: Least-square fitting results of the motions of the maser spot with the LSR velocity of -42.2 km s^{-1}. Top two: least-square fitting using the image peak positions. Bottom two: least-square fitting using the two dimensional Gaussian peak positions. Left panels show the maser positions after removing the initial position and the proper motions.

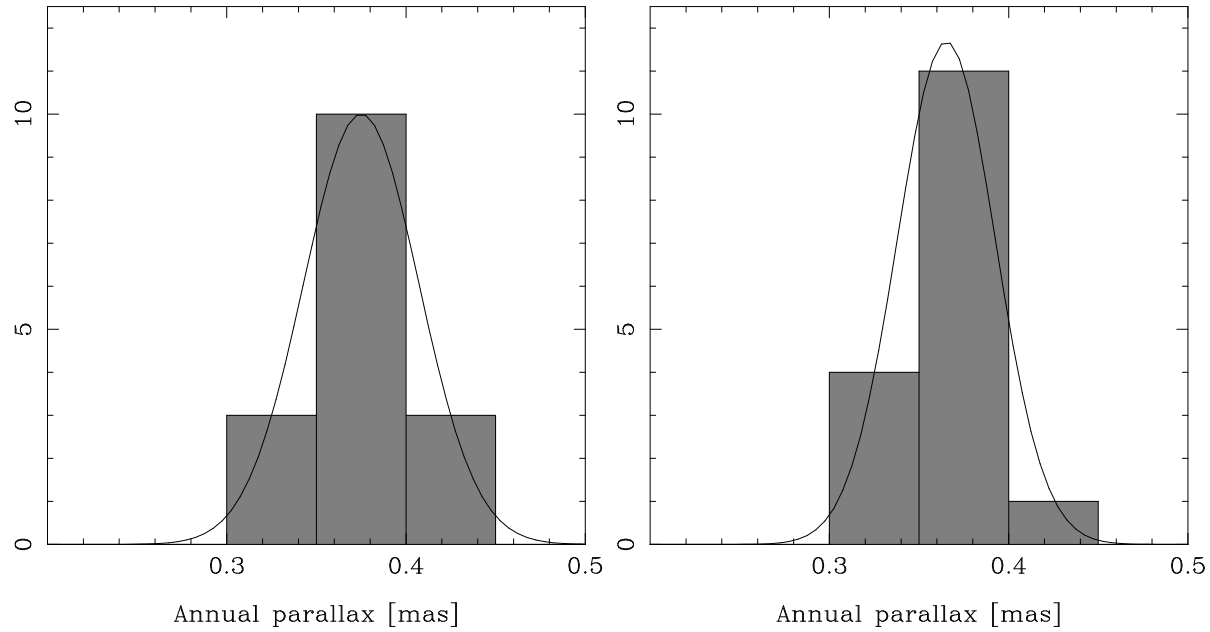

Figure 2.15: Histograms of individual annual parallaxes for 16 maser spots. Left: histogram for the case that the maser spot positions are measured with the image peak positions. The solid line represent a Gaussian fitting curve with the histogram. The 1-σ of the Gaussian curve is 0.046 mas. Right: the same as the left panel but for the case that the maser spot positions were measured with the Gaussian peak positions, and the 1-σ is 0.039 mas.

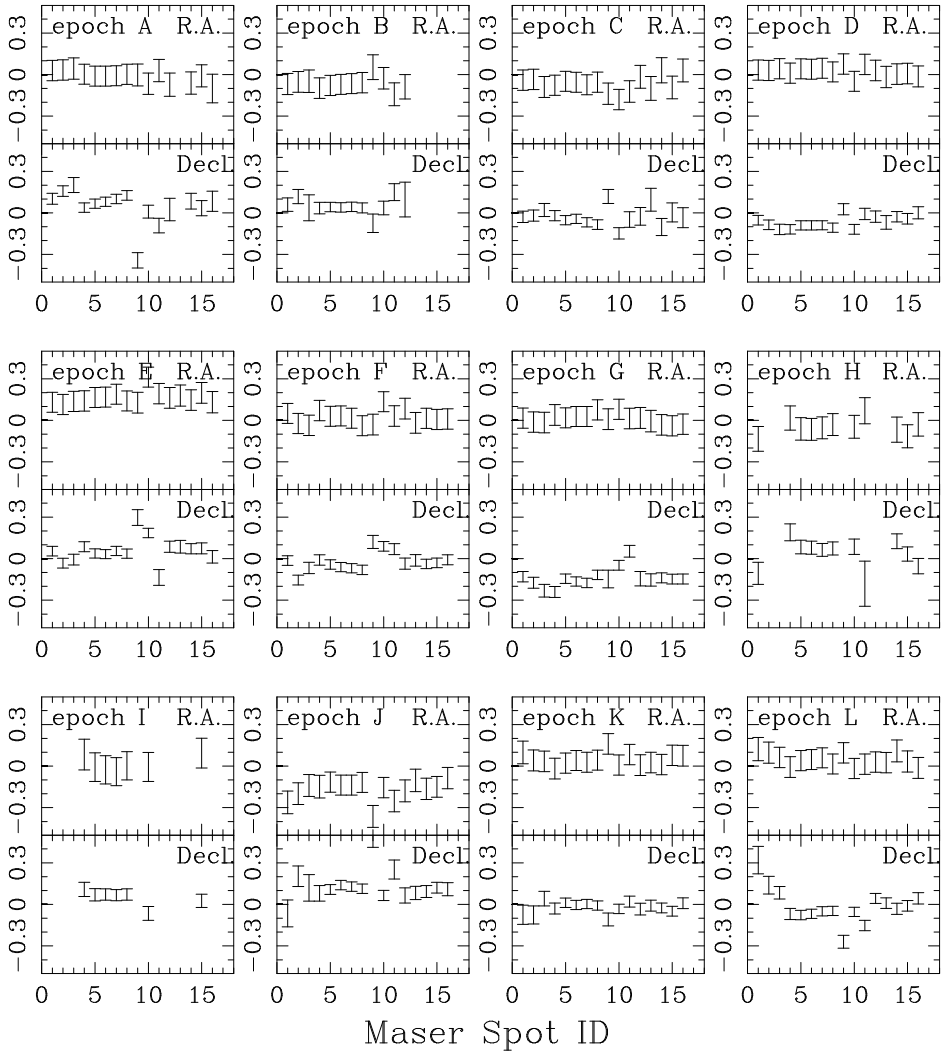

Figure 2.16: Position residuals of the 16 maser spots after removing the annual parallax of 0.356 mas, proper motions, and initial positions. The abscissa represents the maser spot ID as shown in Figures 2.12 and 2.13, and the ordinate is the position residual in mas. For each epoch, the position residuals in right ascension and declination are shown in the upper and lower panel, respectively.

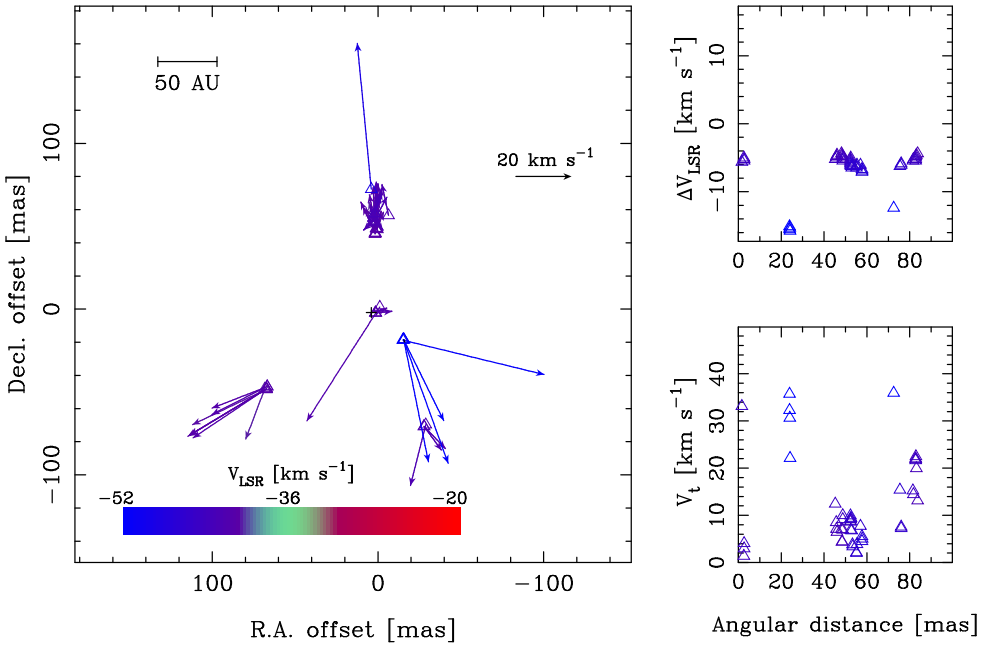

Figure 2.17: Internal motions of maser spots around PZ Cas. The cross bars around the map origin represent the position of PZ Cas and its positional error obtained the least square fitting. The color represents the radial velocity, and open circles and triangles are red- and blue-shifted maser spots with respect to the systemic velocity. Left: spatial distributions of the maser spots with respect to the stellar position (coordinate origin). Right upper: radial velocity – position plot. The abscissa is the angular distance from the stellar position, and the ordinate is the radial velocity difference from the systemic velocity. Right bottom: transverse velocity – position plot.

Table 2.1: Observing epochs of PZ Cas astrometric monitoring observations

Epoch	Date	Time range (UTC)
A	2006 Apr 20	19:41 – 05:20
B	2006 Jul 14	14:21 – 23:10
C	2006 Aug 13	12:21 – 21:35
D	2006 Oct 19	08:01 – 17:20
E	2006 Dec 13	04:21 - 13:40
F	2007 Mar 22	00:21 – 08:17
G[a]	2007 May 2	18:51 – 04:40
H[b]	2007 Jul 25	13:20 – 23:04
I [c]	2007 Sep 19	10:20 – 20:10
J	2007 Nov 7	07:20 – 17:10
K	2007 Dec 22	04:25 – 14:15
L	2008 May 12	19:00 – 04:50

[a] Signal-to-noise ratio for all the baselines were unexpectedly low.

[b] $T_{\rm sys}$ data of ISHIGAKI was used as that of OGASA20.

[c] IRIKI did not attend the observation.

Table 2.2: Frequency allocation for PZ Cas and J2339+6010 at epoch F

Beam	A	B
Source	PZ Cas	J2339+6010
Base band number	1	14
Frequency range [GHz]	22.234 – 22.242	22.106 – 22.122 22.122 – 22.138 22.138 – 22.154 22.154 – 22.170 22.170 – 22.186 22.186 – 22.202 22.202 – 22.218 22.234 – 22.250 22.250 – 22.266 22.266 – 22.282 22.282 – 22.298 22.298 – 22.314 22.314 – 22.330 22.330 – 22.346
Frequency spacing	15.625 kHz[a] (512 chnnels)	250.0 kHz (64 channels)

[a] The velocity spacing of A-beam for the H_2O masers is 0.2107 km s^{-1}.

Table 2.3: Phase tracking center positions of the observed sources

	Right Ascension (J2000)	Declination (J2000)
PZ Cas	$23^{\rm h}44^{\rm m}03^{\rm s}.281900$	$+61^\circ47'22''.182000$
J2339+6010	$23^{\rm h}39^{\rm m}21^{\rm s}.125210$	$+60^\circ10'11''.849000$

Table 2.4: Annual parallax results (mas) of PZ Cas

Spot identification method	Blended component	Isolated component	All
Image peak	0.402 ± 0.021	0.371 ± 0.013	0.380 ± 0.011
2-D Gaussian peak	0.352 ± 0.017	0.358 ± 0.013	0.356 ± 0.011

Table 2.5: Proper motions, initial positions, and parallaxes of the PZ Cas H_2O maser spots

Spot ID (Group ID)	$\Delta\alpha_A$ [mas]	$\Delta\delta_A$ [mas]	V_{LSR} [km s^{-1}]	π [mas]	$\mu_\alpha \cos\delta$ [mas yr^{-1}]	μ_δ [mas yr^{-1}]
1(a)	-4.24 ± 0.07	52.24 ± 0.03	-40.9	0.324 ± 0.042	-3.79 ± 0.06	-1.66 ± 0.03
2(a)	-4.20 ± 0.07	52.40 ± 0.04	-41.2	0.379 ± 0.044	-3.70 ± 0.06	-1.46 ± 0.03
3(a)	-4.07 ± 0.07	52.70 ± 0.04	-41.4	0.340 ± 0.044	-3.72 ± 0.06	-1.30 ± 0.03
4(a)	-2.77 ± 0.07	56.32 ± 0.04	-41.4	0.380 ± 0.039	-3.67 ± 0.06	-1.34 ± 0.03
5(a)	-2.83 ± 0.07	56.29 ± 0.03	-41.6	0.357 ± 0.039	-3.72 ± 0.06	-1.33 ± 0.03
6(a)	-2.82 ± 0.07	56.28 ± 0.03	-41.8	0.363 ± 0.038	-3.73 ± 0.06	-1.30 ± 0.03
7(a)	-2.83 ± 0.07	56.32 ± 0.03	-42.0	0.357 ± 0.038	-3.76 ± 0.06	-1.30 ± 0.03
8(a)	-2.90 ± 0.07	56.32 ± 0.03	-42.2	0.355 ± 0.039	-3.74 ± 0.06	-1.25 ± 0.03
9(a)	-2.62 ± 0.07	56.62 ± 0.03	-42.4	0.302 ± 0.039	-3.78 ± 0.06	-1.28 ± 0.03
10(a)	-2.49 ± 0.07	56.70 ± 0.04	-42.6	0.355 ± 0.046	-3.95 ± 0.06	-1.53 ± 0.03
11(a)	-2.39 ± 0.08	58.82 ± 0.05	-42.2	0.436 ± 0.045	-3.74 ± 0.06	-1.81 ± 0.03
12(a)	-2.27 ± 0.07	58.65 ± 0.04	-42.4	0.349 ± 0.043	-3.69 ± 0.06	-1.82 ± 0.03
13(a)	-3.14 ± 0.07	61.47 ± 0.04	-43.1	0.357 ± 0.051	-3.81 ± 0.08	-1.62 ± 0.03
14(b)	63.82 ± 0.07	-45.57 ± 0.03	-40.9	0.367 ± 0.044	-2.28 ± 0.07	-2.86 ± 0.03
15(b)	63.75 ± 0.07	-45.49 ± 0.03	-41.2	0.349 ± 0.041	-2.30 ± 0.07	-2.85 ± 0.03
16(b)	63.70 ± 0.07	-45.46 ± 0.04	-41.4	0.335 ± 0.044	-2.32 ± 0.07	-2.84 ± 0.03

Table 2.6: Proper motions and initial positions of the maser spots detected at least in two epochs[a]

Spot ID (Group ID)	$\Delta\alpha_A$ [mas]	$\Delta\delta_A$ [mas]	V_{LSR} [km s^{-1}]	$\mu_\alpha \cos\delta$ [mas yr^{-1}]	μ_δ [mas yr^{-1}]
17(a)	-2.99 ± 0.09	49.94 ± 0.06	-40.5	-3.72 ± 0.24	-1.63 ± 0.11
18(a)	-2.99 ± 0.09	49.85 ± 0.06	-40.7	-3.60 ± 0.20	-1.57 ± 0.09
19(a)	-3.02 ± 0.08	49.79 ± 0.08	-40.9	-3.62 ± 0.20	-1.59 ± 0.10
20(a)	-3.05 ± 0.08	49.83 ± 0.09	-41.2	-3.67 ± 0.20	-1.64 ± 0.10
21(a)	-3.13 ± 0.09	49.99 ± 0.15	-41.4	-3.78 ± 0.27	-0.73 ± 0.11
22(a)	-4.36 ± 0.08	52.05 ± 0.05	-40.5	-3.87 ± 0.12	-1.45 ± 0.06
23(a)	-4.28 ± 0.07	52.09 ± 0.04	-40.7	-3.80 ± 0.07	-1.72 ± 0.03
24(a)	-3.78 ± 0.08	52.46 ± 0.07	-41.6	-3.81 ± 0.09	-1.29 ± 0.03
25(a)	-2.66 ± 0.09	56.15 ± 0.06	-41.2	-3.60 ± 0.08	-1.48 ± 0.04
26(a)	-1.42 ± 0.07	57.46 ± 0.04	-42.4	-3.59 ± 0.42	-1.79 ± 0.28
27(a)	-2.25 ± 0.07	56.82 ± 0.03	-42.2	-4.13 ± 0.19	-2.04 ± 0.09
28(a)	-2.19 ± 0.08	58.48 ± 0.05	-42.6	-3.70 ± 0.07	-1.82 ± 0.03
29(a)	-3.02 ± 0.10	61.42 ± 0.07	-42.6	-3.67 ± 0.13	-1.70 ± 0.04
30(a)	-3.04 ± 0.09	61.32 ± 0.04	-42.8	-3.84 ± 0.09	-1.59 ± 0.03
31(a)	-3.08 ± 0.08	61.35 ± 0.04	-43.3	-3.80 ± 0.08	-1.68 ± 0.03
32(b)	63.78 ± 0.09	-45.68 ± 0.06	-40.5	-1.71 ± 0.17	-3.08 ± 0.06
33(b)	63.92 ± 0.07	-45.71 ± 0.04	-40.7	-2.26 ± 0.07	-2.70 ± 0.03
34(b)	63.74 ± 0.08	-45.52 ± 0.05	-41.6	-2.34 ± 0.10	-2.85 ± 0.04
35(b)	60.50 ± 0.10	-44.46 ± 0.08	-41.2	-1.53 ± 0.70	-3.30 ± 0.04
36(b)	62.97 ± 0.08	-43.86 ± 0.05	-41.4	-2.70 ± 0.08	-2.31 ± 0.04
37(b)	63.00 ± 0.08	-43.74 ± 0.06	-41.6	-2.72 ± 0.10	-2.54 ± 0.04
38(c)	-31.47 ± 0.10	-66.14 ± 0.17	-42.0	-4.07 ± 0.17	-2.40 ± 0.05
39(c)	-31.48 ± 0.09	-66.14 ± 0.10	-42.2	-4.03 ± 0.15	-2.44 ± 0.05
40(c)	-33.02 ± 0.10	-67.47 ± 0.07	-42.4	-4.00 ± 0.30	-2.87 ± 0.06
41(d)	0.03 ± 0.08	77.85 ± 0.06	-48.3	-1.95 ± 1.44	-0.35 ± 0.17
42(d)	-0.06 ± 0.08	78.28 ± 0.06	-48.5	-3.42 ± 1.37	0.71 ± 0.17
43(g)	-3.97 ± 0.08	1.15 ± 0.05	-41.2	-3.77 ± 1.04	-1.95 ± 0.11
44(g)	-3.98 ± 0.08	1.06 ± 0.05	-41.4	-3.87 ± 0.27	-1.97 ± 0.05
45(g)	-3.89 ± 0.09	1.12 ± 0.06	-41.6	-4.00 ± 0.15	-1.98 ± 0.04
46(g)	-6.51 ± 0.09	0.67 ± 0.07	-41.8	-2.38 ± 1.61	-4.09 ± 0.05

[a] Maser spots listed in Table 2.4 are excluded.

Table 2.7: Astrometry analysis results of PZ Cas

Annual parallax	$\pi^* = 0.356 \pm 0.026$ mas ($2.81^{+0.22}_{-0.19}$ kpc)	
Position (J2000)[a]	Right Ascension:	Declination:
(2006 Apr 20)	$23^{\rm h}44^{\rm m}03^{\rm s}.2816 \pm 0^{s}.0004$	$+61^\circ47'22''.187 \pm 0''.003$
Stellar proper motion	$\mu^*_\alpha \cos\delta = -3.7 \pm 0.2$ mas yr^{-1}	$\mu^*_\delta = -2.0 \pm 0.3$ mas yr^{-1}

[a] The position errors of J2339+6010 is not taken into consideration. This position is located at the origin of PZ Cas image of Figure 2.11.

Chapter 3

Discussions

3.1 Distance to PZ Cas and Cas OB5

We obtained the trigonometric parallax to PZ Cas, $D = 2.81^{+0.22}_{-0.19}$ kpc as described in Chapter 2. PZ Cas is thought to be a member of the Cas OB5 association in the Perseus spiral arm. It is of interest to compare the distance to PZ Cas determined in this thesis and that has been accepted by other methods. Mel'nik & Dambis (2009) estimated the trigonometric parallax to Cas OB5 to be 2.0 kpc from the median of trigonometric parallaxes of the member stars obtained with *Hipparcos*. Since a typical statistical error of *Hipparcos* annual parallaxes is ~ 1 mas, we cannot fully rely on this statistical value for the object. Another estimate of the distance to Cas OB5 is a distance modulus of 12, corresponding to the photometric parallax of 2.5 kpc (Humphreys 1978). VLBI phase referencing astrometry has revealed that its measured trigonometric parallaxes for RSGs are well consistent with photometric parallaxes of the related star clusters within $10-20$ % (S Per, Asaki et al. 2010; VY CMa, Zhang et al. 2012a; NML Cyg, Zhang et al. 2012b). Therefore, it is highly plausible that PZ Cas is involved in Cas OB5 from the geometrical view of point.

On the other hand, the difference between the distances derived from PZ Cas's annual parallax and from the photometric parallax of Cas OB5 is too large to be explained from the viewpoint of its extent in depth, comparing with the distribution on the sky of the member stars. One of the plausible reasons for the inconsistency is overestimation of $A_{\rm V}$ to Cas OB5. If we attribute the inconsistency to the $A_{\rm V}$ value, the difference is 0.16 magnitude, which comparable to a typical statistical error of $A_{\rm V}$.

3.2 The location of PZ Cas in the H-R diagram

The bolometric luminosity, $L = 4\pi D^2 F_{\rm bol}$, of PZ Cas was estimated to be $2.0 \times 10^5 L_\odot$, $2.1 \times 10^5 L_\odot$, and $1.9 \times 10^5 L_\odot$ by Josselin et al. (2000), Levesque et al. (2005), and Mauron & Josselin (2011) with the distance modulus of Cas OB5 of 12 (Humphreys 1978). To derive the mass and age of PZ Cas, we first re-scaled the luminosity values with our trigonometric parallax to $2.5 \times 10^5 L_\odot$, $2.7 \times 10^5 L_\odot$, and $2.4 \times 10^5 L_\odot$, respectively. Levesque et al. (2005) estimated the effective temperature of PZ Cas to be 3600 K from the MARCS stellar atmosphere models and the absolute spectro-photometry. Using this effective temperature we plot PZ Cas in the H-R diagram reported by Meynet & Maeder (2003) as shown in Figure 3.1. In this figure, filled circles represent the re-estimated luminosities based on Josselin et al. (2000), Levesque et al. (2005), and Mauron & Josselin (2011) while open circles represent the originally reported ones. The luminosity previously estimated by using the distance modulus yields the initial mass of around 20 $M_\odot$ while, using our trigonometric parallax, it is estimated to be $\sim$25 $M_\odot$.

According to evolutionary tracks shown in Figures 1 and 2 of Meynet & Maeder (2003), the lifetime is estimated to be $\sim$ 8 Myr for an initial mass of 25 $M_\odot$ while $\sim$ 10 Myr for an initial mass of 20 $M_\odot$. Since ages of four open clusters in Cas OB5 have been reported to be 120 ± 20 Myr for NGC 7790 (Gupta et al. 2000), and 30.2, 45.7, and 13.2 Myrs for NGC 7788, Frolov 1, and King 12, respectively (Kharchenko et al. 2005), it is expected that PZ Cas was born after the first generation in Cas OB5.

3.3 Three dimensional motion of PZ Cas in the Milky Way

The stellar proper motion and the radial velocity of PZ Cas enable us to discuss its 3-D motion in the Milky Way. In the analysis we adopted the Galactocentric distance to the Sun of 8.5 kpc, and the flat Galactic rotation curve with the rotation velocity of 220 km s^{-1}. For the Solar motion, we adopted the latest value obtained by Schönrich et al. (2010), 11.10 ± 0.75 km s^{-1} toward the direction of the Galactic center ($U_\odot$ component), 12.24 ± 0.47 km s^{-1} toward the direction of the Galactic rotation ($V_\odot$ component), and 7.25 ± 0.37 km s^{-1} toward the Galactic north pole ($W_\odot$ component). Since H_2O maser features around RSGs are spherically distributed, it is hardly plausible that an uncertainty in the stellar proper motion because of the the anisotropic distribution as those in the case of outflows of star-forming regions has to be considered (e.g., Sanna et al. 2009). Therefore we did not introduce an additional uncertainty of the PZ Cas stellar motion other than the statistical error described in Chapter 2 in this error estimation. We followed methods described by Johnson & Soderblom (1987) and Reid et al. (2009b) to derive the peculiar

motion. The resultant peculiar motion of PZ Cas is (U_s, V_s, W_s)= (22.8 ± 4.4, 7.1 ± 2.2, −5.7 ± 4.0) km s^{-1}. We have to note that the error in the peculiar motion was evaluated based on error propagation from the errors of the annual parallax and proper motion (Johnson & Soderblom 1987).

Figure 3.2 shows spatial position and the peculiar motion of of PZ Cas and other maser sources projected on the Galactic plane. The peculiar motion of PZ Cas is as large (>10 km s^{-1}) in the same manner as Galactic HMSFRs and young stars which have already been reported (Reid et al. 2009b; Baba et al. 2009). Large U_s component is consistent with the characteristics of the peculiar motion of sources on the Perseus arm (Sakai et al. 2012). However, since the peculiar motion of PZ Cas has a positive V_s component, it is different from the trend of sources of Perseus arm Figure 3.3. There are NGC281W in the same trend as PZ Cas, the origin of peculiar motion is due to the expansion motion of the super bubble in those areas (Sato et al. 2008; Sakai et al. 2013).

We here consider three possibilities to cause such a large peculiar motion of PZ Cas as follows:

(1) PZ Cas has an exceptionally large peculiar motion such as a runaway star in the star cluster, Cas OB5 (runaway star hypothesis);

(2) the member stars in the OB association have systematic velocity due to an expanding motion of the supershell (supershell hypothesis); and

(3) Galactic young objects universally have a large peculiar motion due to epicyclic motions in the Galactic dynamics (epicyclic motion hypothesis in galaxy dynamics).

In the following, we investigate the above three hypotheses to search for the origin of the peculiar motion of PZ Cas.

3.3.1 Runaway Star Hypothesis

We here examined the first hypothesis that PZ Cas is a runaway star. A runaway star has relatively higher peculiar motion (> 30 km s^{-1}) than that of its surrounding stars. Blaauw (1961) reported that about 20% of O-type stars and 5% of B-type stars are runaway stars in the solar neighborhood. Schilbach and Röumlser (2008) showed that 90% of the runaway stars originate from OB associations or star clusters. Fujii & Zwart (2011) presented their theoretical study results that runaway stars are produced by the gravitational interaction in young star clusters (OB associations). In order to elucidate this hypothesis for the peculiar motion of PZ Cas, we firstly compared the apparent motion of PZ Cas to those of the member stars involved in Cas OB5. We obtained proper motions of the member stars of Cas OB5 from the *Hipparcos* catalogue (Høg et al. 2000). Positions and velocities of fifteen Cas OB5 member stars (OB stars and

RSGs) catalogued in Garmany & Stencel (1992) with compiled information from previous literatures (Wilson 1953; Evans 1967; Humphreys 1970; Fehrenbach et al. 1996; Valdes et al. 2004; Famaey et al. 2005; Van Leeuwen F. 2007) are listed in Table 3.1. Figure 3.4 shows the positions and proper motions of the member stars listed in Table 3.1 as well as stars with annual parallax < 5 mas and proper motion < 8 mas yr^{-1} in the *Hipparcos* catalogue in order to roughly exclude foreground stars. In Figure 3.4, $J = 1 \rightarrow 0$ CO contour map of a Galactic plane survey (Dame et al. 2001) taken from *SkyView* (Internet's Virtual Telescope) [1] is superimposed. We obtained unweighted average of those proper motions ($\mu_\alpha \cos\delta = -2.8 \pm 1.2$, and $\mu_\delta = -1.9 \pm 0.8$ mas yr^{-1}) which is well consistent with Cas OB5's peculiar motion obtained by Mel'nik & Dambis (2009) ($\mu_\alpha \cos\delta = -3.8 \pm 1.2$, and $\mu_\delta = -1.4 \pm 0.8$ mas yr^{-1}). The proper motion of PZ Cas obtained in this study is consistent with the average of those of the fifteen member stars with the margins of error. We secondly compared peculiar motions between PZ Cas obtained in this study and fourteen of the fifteen stars whose radial velocities have been measured. In the comparison, we adopted $2.81\ ^{+0.22}_{-0.19}$ kpc for distances of all the member stars of Cas OB5. The average of the peculiar motion of the fourteen sources and the standard deviation are $(\overline{U}_{\rm OB5}, \overline{V}_{\rm OB5}, \overline{W}_{\rm OB5}) = (18 \pm 14, -1 \pm 18, -9 \pm 18)$ km s^{-1}. Figure 3.5 shows histograms of each of the three components of the peculiar motions (U, V, W) of the fourteen stars. From the histograms, we noted that there are two stars with very large peculiar motions: $(9 \pm 9, -40 \pm 7, -32 \pm 9)$ and $(34 \pm 21, -38 \pm 12, 39 \pm 27)$ km s^{-1} for HD224424 and KN Cas, respectively. Because spectral types of these two sources are available the distances can be judged not to be very close to the Sun comparing with the other member stars. Therefore, it is not possible to attribute such large peculiar motions to the location of the stars (foreground stars). We consider those stars are a type of runaway stars. Figure 3.6 shows the same histogram but removing HD224424 and KN Cas. We obtained the peculiar motion except HD224424 and KN Cas: $(\overline{U}'_{\rm OB5}, \overline{V}'_{\rm OB5}, \overline{W}'_{\rm OB5}) = (18 \pm 14, 5 \pm 9, -11 \pm 11)$ km s^{-1}. It is clear that the peculiar motion of PZ Cas is almost located at around the median of the distribution, $(\tilde{U}, \tilde{V}, \tilde{W}) = (22.8, 7.1, -5.7)$ km s^{-1}. From the above two analyses, we concluded that PZ Cas has a typical peculiar motion in Cas OB5 and that the runaway star hypothesis for PZ Cas can be rejected. This tentative conclusion indicates that Cas OB5 has a large peculiar motion.

3.3.2 Supershell Hypothesis

Next, we examined the second hypothesis coming from the expansion motion of the supershell. A supershell is a large shell-like gas structure which is considered to be swept up by radiation pressure from precedent OB stars and/or supernova explosions. Fich (1986)

[1] SkyView web: http://skyview.gsfc.nasa.gov/

found an H_I supershell whose western side is located at the position of Cas OB5. Moór & Kiss (2003) reported that the H_I supershell has the radius of $\sim$ 190 pc, the expansion velocity of $\sim$ 20 km s^{-1}, and the total amount of mass swept up of 7.5×10^5 $M_\odot$. In order to see whether Cas OB5's peculiar motion is related to the expansion motion of the supershell, we investigated the peculiar motion of Cas OB5 by comparing with those of Cas OB4 and Cas OB7 which are located on the eastern side of the supershell. Positions, proper motions measured with *Hipparcos*, and radial velocities of the member stars of Cas OB4 and Cas OB7 are listed in Table 3.2. Figure 3.4 shows the proper motions of the member stars of Cas OB4, Cas OB5, and Cas OB7. We cannot find any clear evidence that the member stars of the three OB associations are expanding in their proper motions.

We also investigated 3-D relative positions and peculiar motions of those of Cas OB4 and Cas OB7. We adopted the photometric parallaxes of 2.9 and 2.5 kpc for Cas OB4 and Cas OB7, respectively (Humphreys 1978). Figure 3.7 shows 3-D views of the positions and peculiar motions of the member stars of Cas OB5 as well as Cas OB4 and Cas OB7. We confirmed from the peculiar motions of those member stars that there is not a simple expanding motion for the member stars of Cas OB4, Cas OB5, and Cas OB7.

Because Cas OB7 is clearly located outside of the supershell, we conducted the following statistical analysis for the peculiar motions of the member stars for Cas OB5 and Cas OB4. Figure 3.8 shows peculiar motions of the member stars of Cas OB5 and Cas OB4 projected on the Galactic plane. For Cas OB4, we calculated the peculiar motions using the *Hipparcos* proper motions and the photometric parallax of 2.88 kpc in both the left and right plots. For Cas OB5, we calculated the peculiar motions from the *Hipparcos* proper motions together with the annual parallax of 2.8 kpc in the left plot, on the photometric parallax of 2.5 kpc in the right plot. PZ Cas's peculiar motion is also plotted for the VLBI astrometric observation result (left) and *Hipparcos* result (right). The error bars for the stars with the *Hipparcos* peculiar motions are calculated with the uniform error of 20 % which is typical error size of the photometric distance. It is quickly noted from Figure 3.8 that the accuracy of the peculiar motion of PZ Cas was much improved with the VLBI phase referencing technique. Using the annual parallax obtained in this research, the velocity dispersion of the Cas OB5 members in the left plot is improved by comparison with the ones shown in the left plot in Figure 3.8.

From the left plot in Figure 3.8, the distribution of the peculiar motions can be divided with a line of $V = -3U$. The average of the peculiar motions and the standard deviation of Cas OB4 are $(\overline{U}_{\rm OB4}, \overline{V}_{\rm OB4}, \overline{W}_{\rm OB4}) = (-11 \pm 10, -4 \pm 14, -15 \pm 8)$ km s^{-1}, and it seem that these two OB associations are moving to the opposite direction each other from an originating point with the peculiar motion of 0. Therefore, the large peculiar motion of PZ Cas and Cas OB5 may be attributed to the expanding motion of the H_I supershell. We have to note that it is difficult to discuss about statistics for these components because

the dispersion is very large.

There are, however, several problems with this hypothesis. The vertical components to the Galactic plane in the peculiar motion of Cas OB5 and Cas OB4 ($\overline{W}_{\rm OB4}$ and $\overline{W}_{\rm OB5}$) are both negative, so that we still need to find a reason for the large negative W components. Another difficulty is the origin of the supershell. Fich (1986) reported that three supernova remnants (SNRs), G114.3+0.3, G116.5+1.1, and CTB1, might produce the supershell. However, because G114.3+0.3 geometrically lies outside of the supershell, G114.3+0.3 is unlikely to affect the supershell from inside. The required energy to produce the supershell was estimated to be 3×10^{52} erg. On the other hand, the typically explosion energy for one supernova is 5×10^{51} erg. The energy from the three SNRs was not enough to form the supershell, we cannot find the energy source to form it.

3.3.3 Epicyclic Motion Hypothesis in Galaxy Dynamics

The density wave hypothesis firstly proposed by Lin & Shu (1964) is a well-known idea to explain spiral arm formation. A star formation is considered to be activated due to gravitational instabilities. In the hypothesis, the density waves traced with spiral arms cause shock fronts which induce triggers of star formation in giant molecular clouds. This hypothesis provides two important predictions in terms of the 3-D motions of young objects in the Milky Way. First, young objects including OB stars are located along with the spiral arms. Secondly, those young objects may have peculiar motions because of the gas flux induced by the density waves. Here let us focus on the second prediction.

According to the hypothesis, there is a corotation radius at which the rotation speeds between the density waves and the matter are equal. Inside the corotation radius, density waves are slower than the galactic rotation while the density waves are faster than the galactic rotation outside the radius. It is considered in the density wave hypothesis that the gas is decelerated when the spiral arm catches up with the density wave outside the corotation radius. It induces the shock front just after passing the density wave and gases will have a peculiar motion with the positive U and negative V components as suggested by Sakai et al. (2012).

The density wave hypothesis provides us a qualitative explanation for the observed peculiar motion of PZ Cas or Cas OB5, and Cas OB4. On the other hand, the problem of this idea is that the quantity of the peculiar motions of PZ Cas and/or the OB associations is much larger than that predicted by the density wave hypothesis: peculiar motions far from the Galactic center will not be over 10 km s^{-1}. In addition, if the VLBI astrometry has showed objects which are located just after they pass the density waves by chance, directions of the peculiar motions should be aligned well. However the reality does not show such a tendency.

The peculiar motion of Cas OB5 hits upon an interesting idea of "time-dependent po-

tential spiral arms". Baba et al. (2009) reported on results of large N-body and smoothed particle hydrodynamics (SPH) simulations that calculated the motions of multi-phase, self-gravity gas particles in self-induced stellar spiral arms in a galactic disk. In their simulations, spiral arms are developed by the self-gravity but cannot keep their forms even in one galactic rotation evolution. Other simulation results by Wada et al. (2011) suggest that a massive cloud falls into a spiral arm's potential from both sides, that is, there are flows of cold gas with various velocities. The flows converge into condensations of cold gas near the bottom of the potential well. The relative velocities of the gas to the stellar spirals are comparable to the random motion of the gas. Another interesting point reported by Wada et al. (2011) is that supernovae feedback is not essential to change the velocity field of the gas near the spiral potential. Each of the cold massive clouds and stars with ages younger than 30 Myr may have a peculiar motion with a velocity dispersion of $\sim$ 30 km s^{-1}, which is not predicted by the density wave theory. Although we have not had samples large enough to discuss the whole structure of the Milky Way, the self-consistent gravity spiral galaxy model can explain those peculiar motions of HMSFRs in the Milky Way. In other words, a live spiral structure model can fit to the recent sample of the HMSFRs' spatial motions including Cas OB5. A deep understanding of the dynamics of the Galactic spiral arms and the origin of the peculiar motions of HMSFRs will be possible in the near future when massive numerical simulations can be combined with much larger VLBI astrometric samples which only can be conducted toward the Galactic plane obscured by dense gas.

3.4 Origin of Large Peculiar Motion of PZ Cas and Future Works

In the previous section, we examined three hypothesis for the large peculiar motion of PZ Cas. We rejected the possibility that PZ Cas is a runaway star escaping from Cas OB5. This suggests that Cas OB5 also has a large peculiar motion. We checked the supershell hypothesis in which stars near the shell regions of the H_I supershell are moving outward from an originating point with zero peculiar motion. Peculiar motions of the member stars of Cas OB5 and Cas OB4 located at the western and eastern edges of the supershell, respectively, shows us that the peculiar motion of PZ Cas can be explained with this hypothesis. On the other hand, there are, however, two difficulties with this hypothesis: one is that W components of peculiar motions of Cas OB5 and another one is the recognized three SNRs cannot generate the supershell, so that we need other energy sources. In the last, we investigated the possibility if PZ Cas has a large peculiar motion in line with the galaxy dynamics. The recent large N-body hydrodynamical simulation study shows that time-dependent spiral arm formation without the density wave is possible and that large

peculiar motion with 20-30 km s^{-1} many happen for GMCs. At this moment, we cannot see which hypothesis in the later two is superior than the other because we don't have a concrete observational evidence.

The last hypothesis is very attractive to explain the peculiar motions of not only PZ Cas but also the other Galactic HMSFRs. The recent N-body hydrodynamical simulations show that the spiral arm formation does not require the density wave which has been considered to play a major role in the spiral galaxies. For a long time since the density wave was proposed, astronomers have pointed out that the density wave cannot maintain the spiral structure without artificial adjustment in numerical simulations. Although we need more samples not in the spiral arms close to the Sun but also many parts of the Milky Way over the Galactic center, the last hypothesis can be the most plausible for the origin of the peculiar motion of PZ Cas.

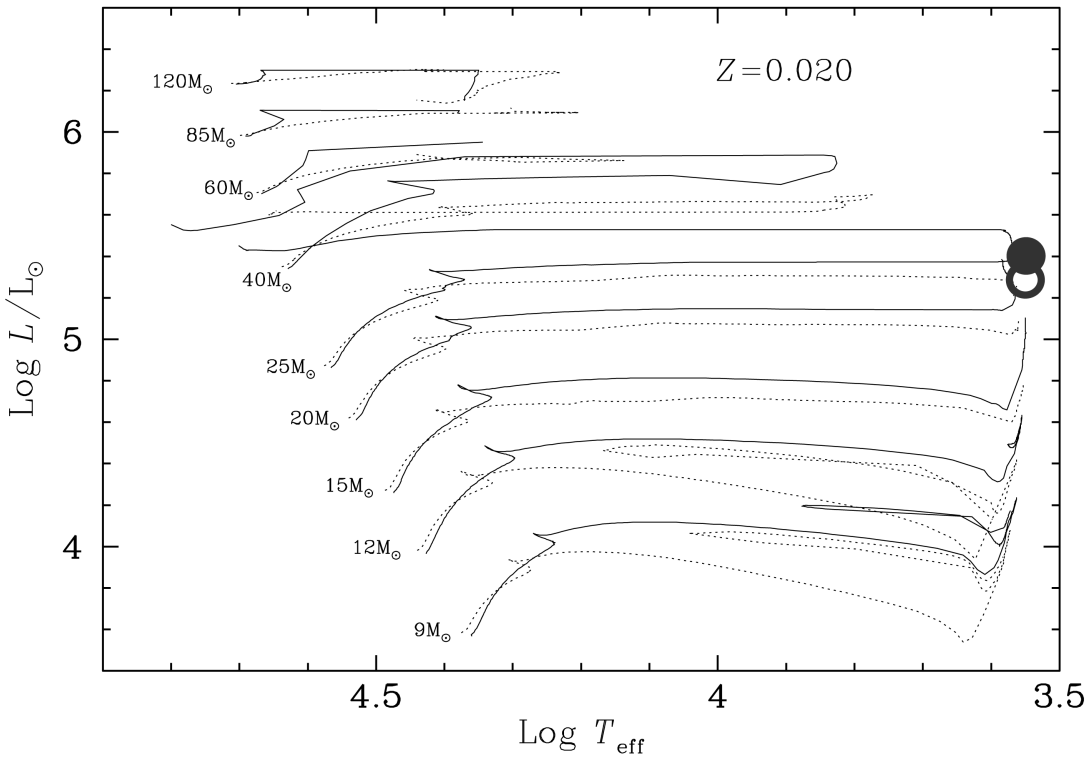

Figure 3.1: Locations of PZ Cas on the H-R diagram. The evolutionary tracks by Meynet & Maeder (2003) are overlaid. The open and filled circles represent the locations of PZ Cas estimated from the distance modulus (Humphreys 1978) and our trigonometric parallax, respectively. The effective temperature is 3600 K (Levesque et al. 2005).

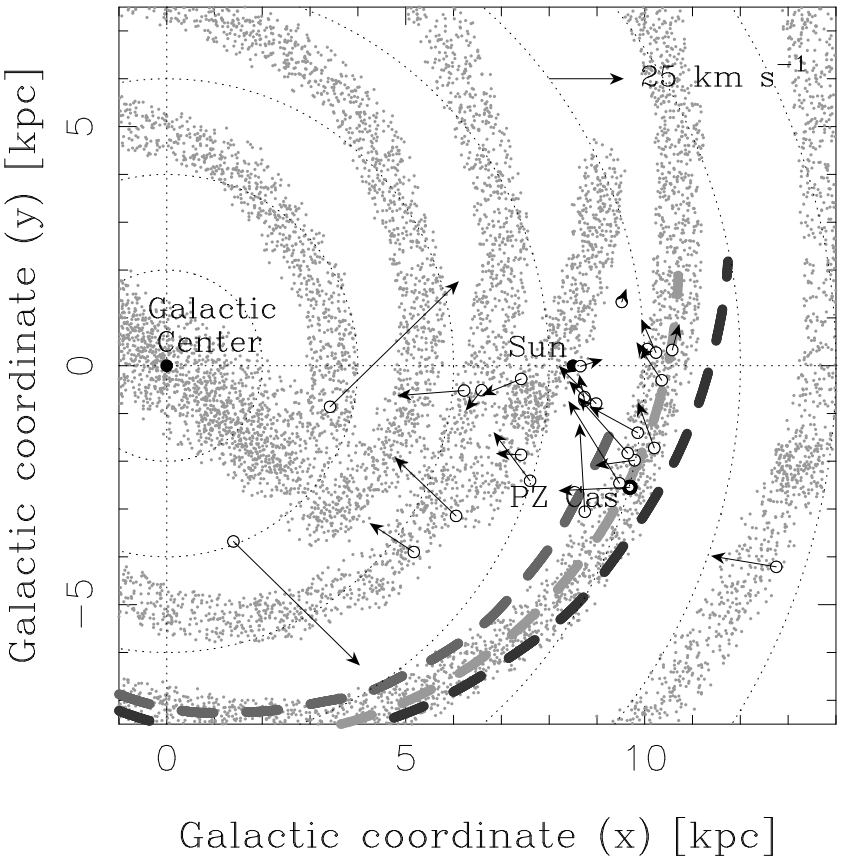

Figure 3.2: Spatial positions and the peculiar motion of U and V components of PZ Cas and other maser sources on the Galactic plane. A dark-gray dashed curve indicates the Perseus arm obtained from the H_{II} survey (Georgelin & Georgelin 1976) while a light-gray dashed curve indicates the one obtained from CO survey (Nakanishi & Sofue 2006). Those traces are adjusted to $R_0 = 8.5$ kpc.

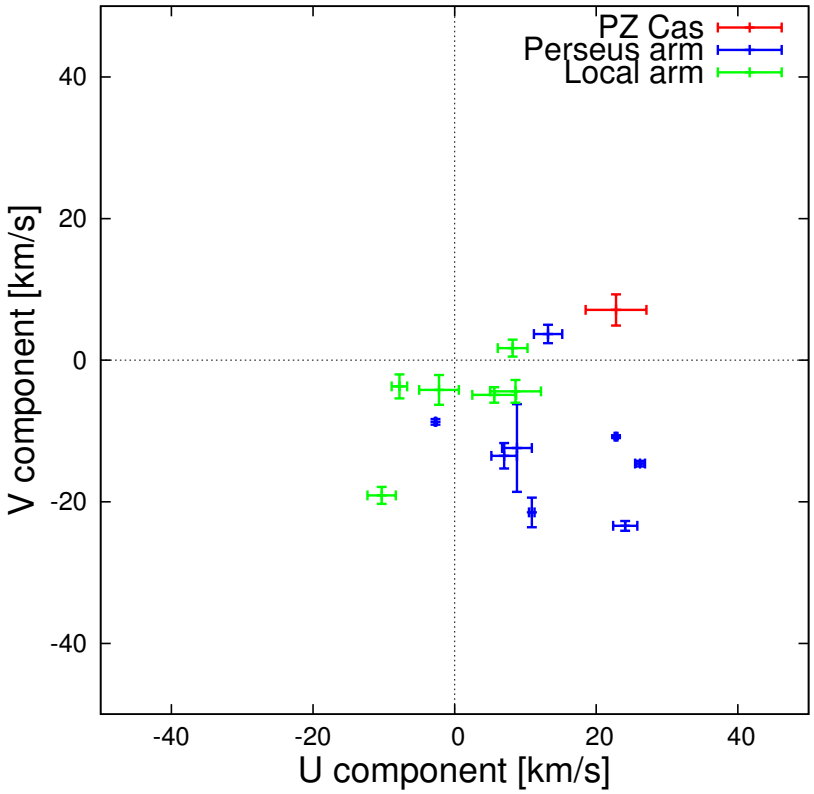

Figure 3.3: Peculiar motions of PZ Cas (red cross), and HMSFRs, S Per, and VY CMa on the Perseus and Local arms represented with blue and green crosses, respectively, projected on the Galactic plane. The peculiar motions of the HMSFRs were calculated from the data listed in Table 6 in Sakai et al. (2012). with the same parameters used for PZ Cas.

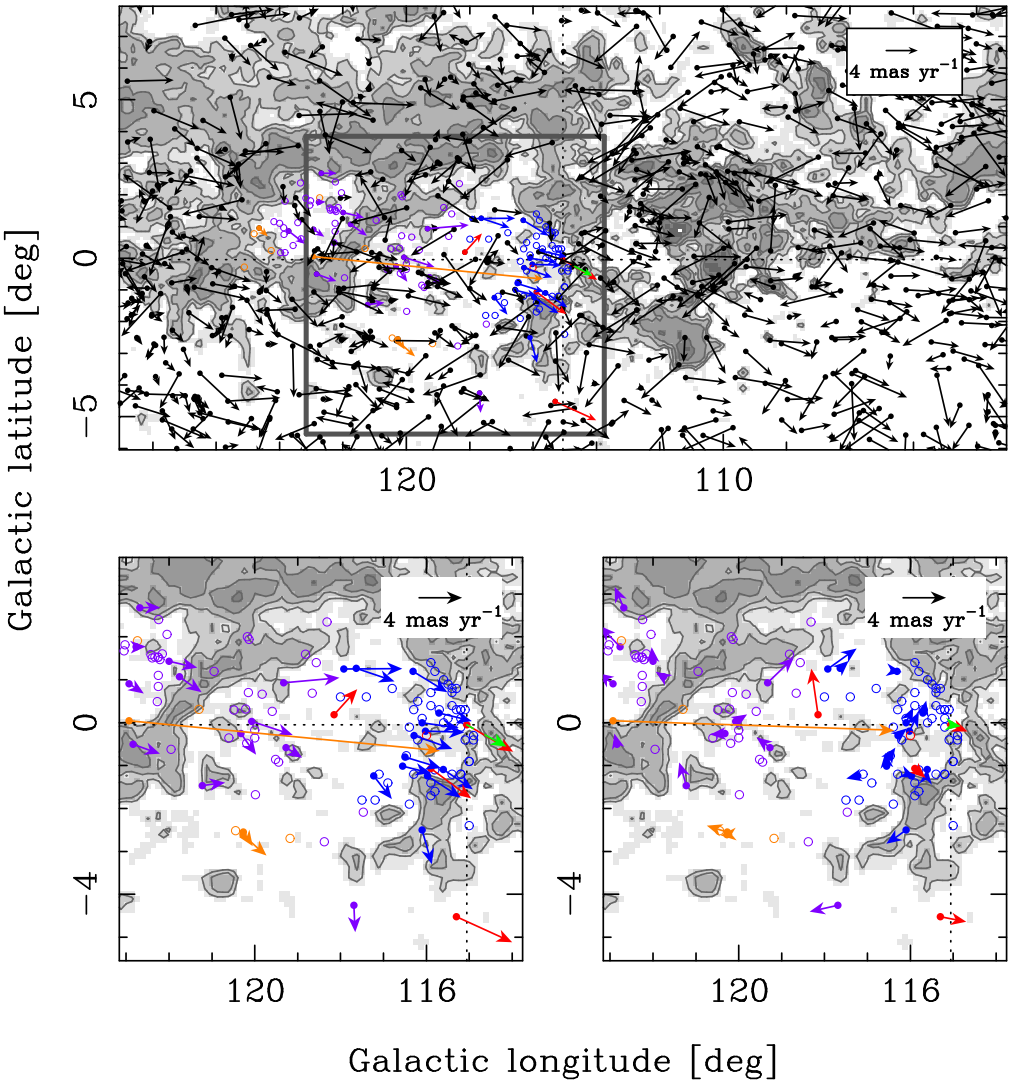

Figure 3.4: Top:proper motions of the Cas OB5, Cas OB4, and Cas OB7 members as well as stars with the annual parallaxes less than 5 mas and the proper motions less than 8 mas yr^{-1} in the *Hipparcos* catalogue. Blue and red circles represent OB stars and RSGs, respectively, which have been identified as Cas OB5 members. The same goes for the Cas OB4 and Cas OB7, and purple and orange circles represent OB stars and RSGs, respectively. Filled and open ones denote the member stars found and not found in the *Hipparcos* catalogue, respectively. Black points denote the stars whose proper motions are reported in the *Hipparcos* catalogue but not identified with a Cas OB5, Cas OB4, and Cas OB7 member. The arrows represent proper motions listed in the *Hipparcos* catalogue. PZ Cas is located at the crossing point of the horizontal and vertical dotted lines. The green arrow represents the proper motion reported in this thesis. The background contour is the CO map by Dame et al. (2001). Bottom left: enlarged picture of the area surrounded by the gray square in the top panel. Bottom right: same as the bottom left but the average proper motion of the Cas OB5 members is subtracted from each proper motion.

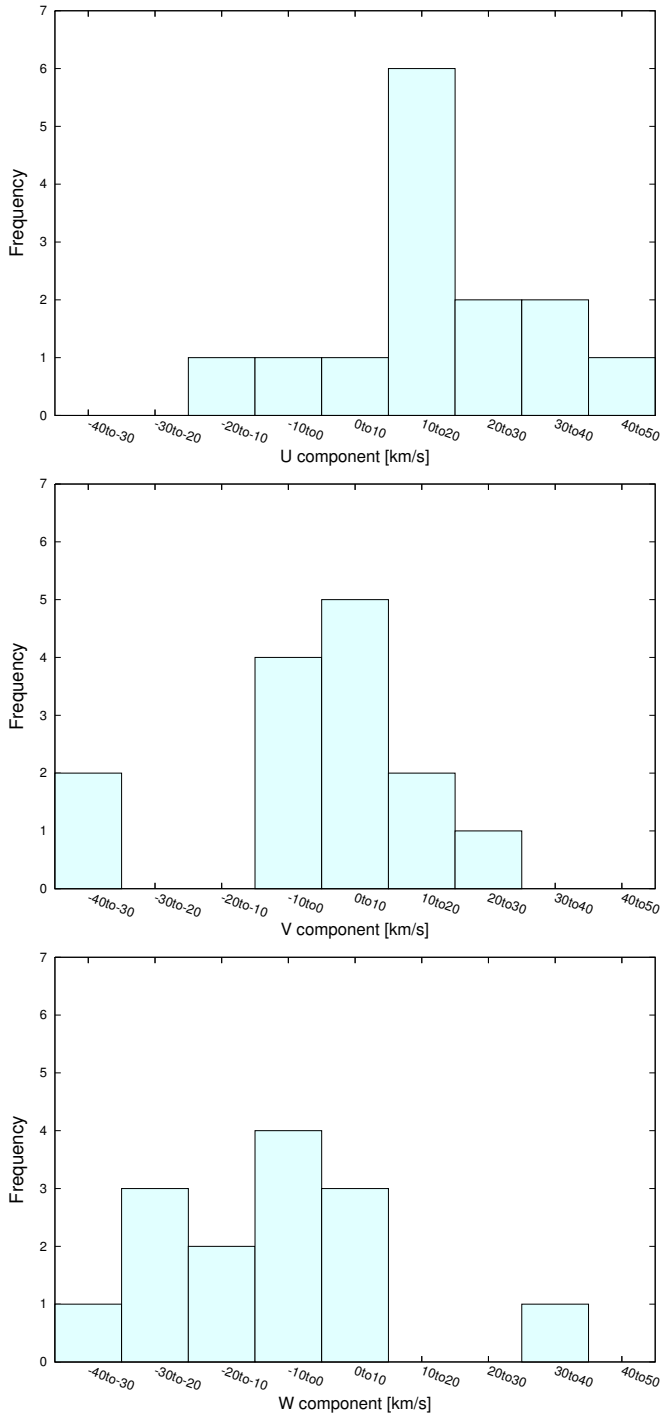

Figure 3.5: Histogram of the peculiar motions from the top to the bottom plot: U, V, and W component for the Cas OB5 members.

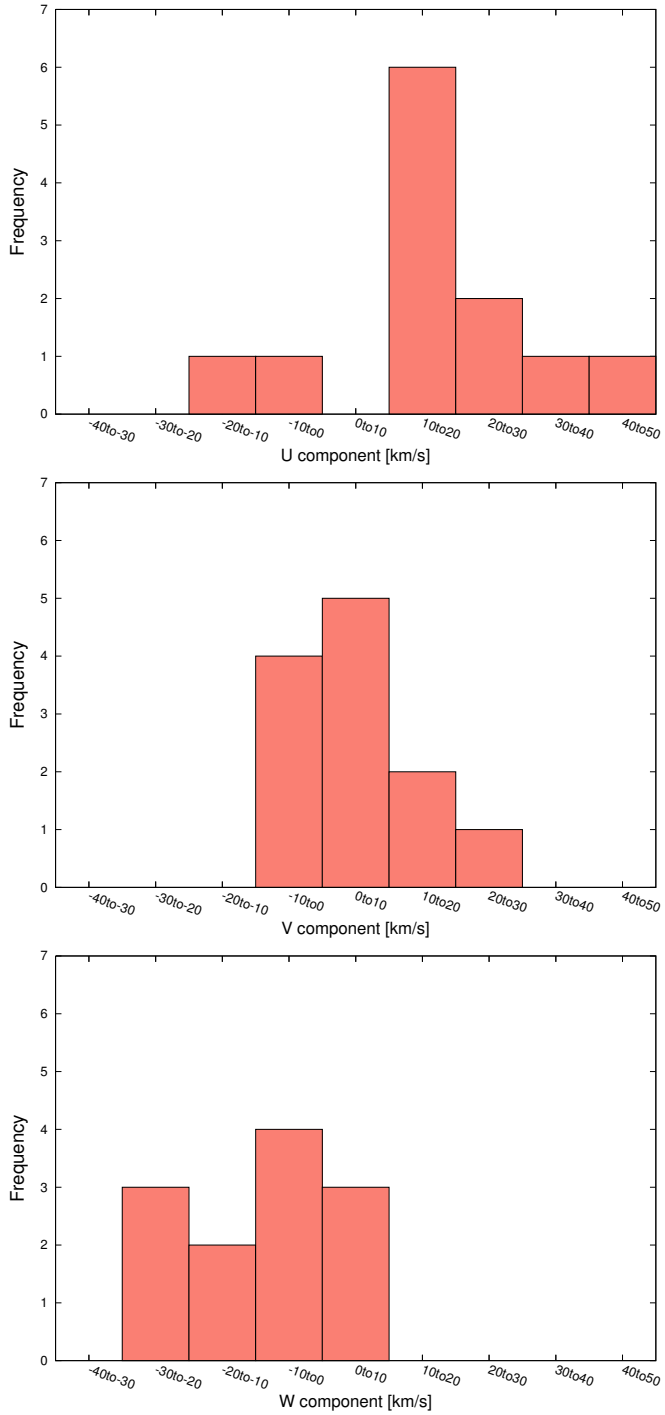

Figure 3.6: The same as Figure 3.5 but removing HD224424 and KN Cas.

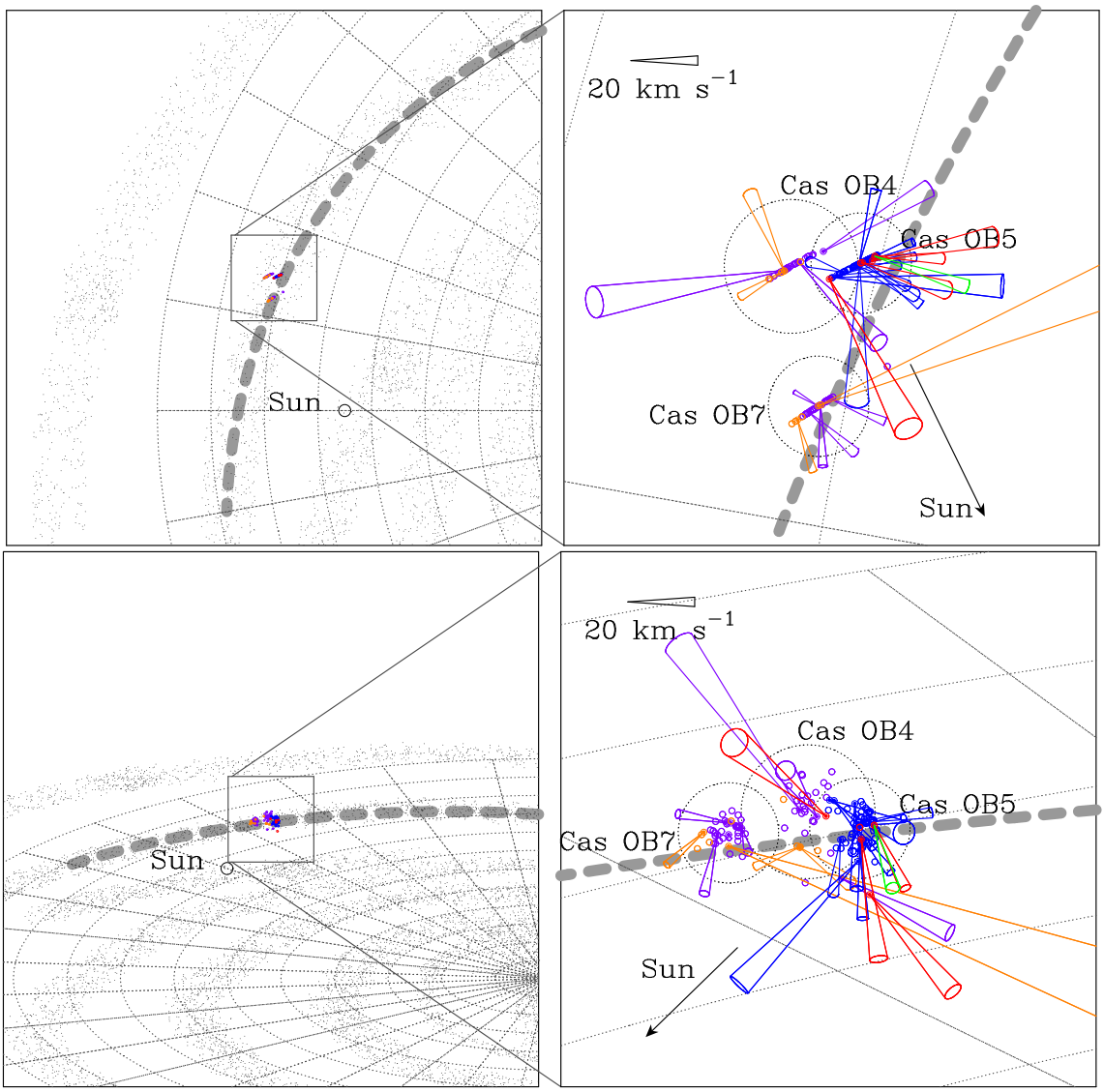

Figure 3.7: Three dimensional views of positions and peculiar motions of the member stars of Cas OB5, Cas OB4 and Cas OB7. Note that the distance to Cas OB5 is assumed to be 2.8 kpc (this paper) while those of Cas OB4 and Cas OB7 are 2.9 and 2.5 kpc, respectively, determined from the photometric parallaxes (Humphreys 1978). Blue and red points are OB stars and RSGs of Cas OB5, respectively, listed in Table 3.1. Green represents PZ Cas's peculiar motion obtained in this paper. Purple and orange are OB stars and RSGs of the other two OB associations, respectively, listed in Table 3.2. Conicals in the enlarged right plots represent the peculiar motions of the member stars after removing the flat Galactic rotation curve of 220 km s^{-1}. A thick grey dashed line represents the position of the Perseus spiral arm (Asaki et al. 2010).

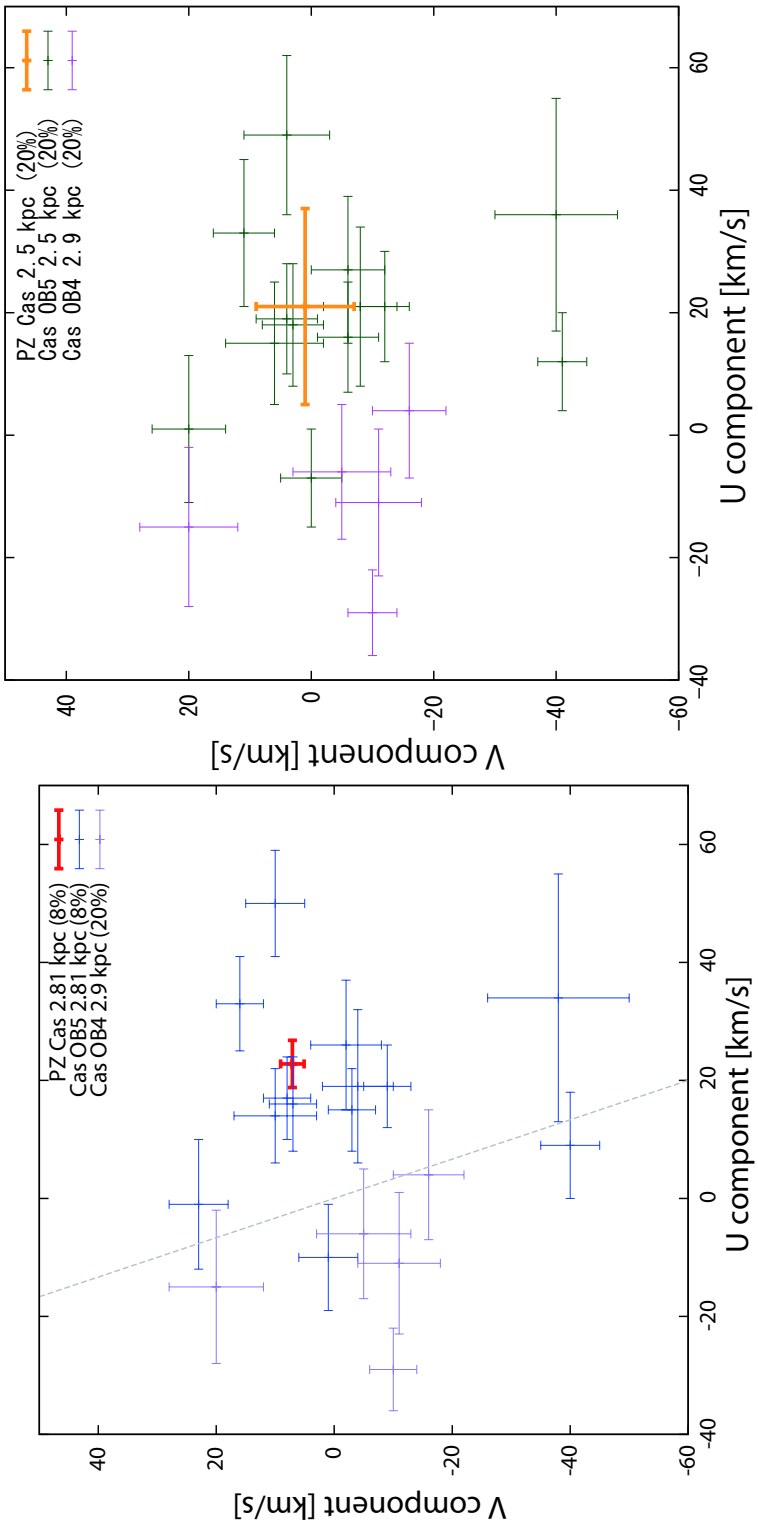

Figure 3.8: Peculiar motions of the member stars of Cas OB5 and Cas OB4. The vertical and horizontal axes are U and V component of the peculiar motion, respectively. Uncertainty of the photometric parallax adopted 20% with respect to the distance. Left panel: the red cross is the peculiar motion of PZ Cas. The blue crosses are peculiar motions of Cas OB5 member stars by assuming. The magenta crosses are calculated for Cas OB4 member stars by using the photometric parallax of 2.88 kpc (Humphreys 1978). Right panel: the green and yellow crosses are calculated the peculiar motions of Cas OB5 member stars and PZ Cas, respectively, by using the photometric parallax of 2.5 kpc (Humphreys 1978). The magenta crosses is the same as the left panel's Cas OB4 member stars.

Table 3.1: Proper motions of the member stars of Cas OB5

Object	l[a] [deg]	b[a] [deg]	$\mu_\alpha \cos\delta$[a] [mas yr^{-1}]	μ_δ[a] [mas yr^{-1}]	V[b] [km s^{-1}]	Spectl type[c]
HD 223385	115.71	0.22	−2.80	−1.45	−55.7[d]	A3 I A+
HD 223767	116.02	−0.20	−3.51	−0.92	−38[e]	A4 I AB
HD 223960	115.97	−1.24	−2.57	−2.67	−48.1[f]	A0 I A+
BD +61 2550	116.08	0.04	−3.22	−1.25	−19[e]	O9.5 II
HD 224424	116.21	−2.45	−0.24	−3.31	−71[f]	B1 I AB
BD +62 2313	116.31	1.20	−2.67	−2.64	−53[e]	B3 I B
HD 224055	116.29	−0.30	−3.22	−1.99	−42.3[f]	B1 I A
LSI +61 106	116.47	−0.77	−3.07	−1.71		B1 V
HD 225146	117.23	−1.24	−1.27	−2.43	−29.0[f]	O9.7 I B
HD 225094	117.63	1.26	−3.27	−1.83	−43[f]	B3 I A
HD 108	117.93	1.25	−5.39	−0.93	−62.8[g]	O5F
ρ Cas	115.30	−4.52	−4.54	−3.45	−43.1[f]	F8 I ap
KN Cas	118.15	0.19	−2.50	2.02	−87.3[h]	M1 I bep+B
TZ Cas	115.90	−1.07	−3.05	−3.56	−54.28[i]	M2 I ab
PZ Cas	115.06	−0.05	−3.52	−3.55	−45.68[i]	M4 I a

[a] Van Leeuwen F. (2007).

[b] Radial velocity (heliocentric coordinate)

[c] Garmany & Stencel (1992).

[d] Valdes et al. (2004).

[e] Fehrenbach et al. (1996).

[f] Wilson (1953).

[g] Evans (1967).

[h] Humphreys (1970).

[i] Famaey et al. (2005).

Table 3.2: Proper motions of the member stars of Cas OB4 and Cas OB7

Object	l[a] (deg)	b[a] (deg)	$\mu_\alpha \cos\delta$[a] (mas yr^{-1})	μ_δ[a] (mas yr^{-1})	V[b] (km s^{-1})	Spectl type[c]
Cas OB4						
HD 1544	119.27	−0.58	−1.38	−1.11	−52.0[d]	B0.5 III
HD 2451	120.32	−0.25	−1.22	−2.11	−37[d]	B0.5 IV
HILTNER 8	117.69	−4.25	0.25	−2.49	−23.5[e]	O9 IV
DL Cas	120.27	−2.55	−0.75	−1.38	−36.80[f]	F7.5 I B
HD 236433	120.28	−2.61	−2.02	−2.12	−11.2[g]	F5 I B
Cas OB7						
HD 3940	122.00	1.44	−2.61	−0.69	−48.0[h]	A1 I A
HD 4694	122.77	1.77	−0.90	0.04	−49.0[i]	B3 I A
HD 4841	122.93	0.91	−1.37	−0.93	−26[e]	B5 I A
HD 5551	123.71	0.85	−2.05	−1.53	−51.0[d]	B1.5 I A
HD 4842	122.93	0.05	−28.98	−2.81	−92[e]	M
HD 6474	124.65	0.95	−1.17	−1.00	−48.3[j]	G4 I A

[a] Van Leeuwen F. (2007).

[b] Radial velocity (heliocentric coordinate)

[c] Garmany & Stencel (1992).

[d] Evans (1967).

[e] Wilson (1953).

[f] Mermilliod et al. (2008).

[g] Kraft (1958).

[h] Münch (1957).

[i] Abt et al. (1972).

[j] Humphreys (1970).

Chapter 4

Conclusions

In this thesis, we have investigated the 3-D motions of one of the RSGs, PZ Cas, to improve our understanding about large peculiar motion of young objects in the spiral arms of the Milky Way. The VERA has conducted the monitor program for the 22 GHz water masers of PZ Cas from 2006 to 2008 by means of the phase referencing VLBI to measure the annual parallax and proper motion. We used the archival data and analyzed 12 epoch observations.

We successfully obtained the spatial distribution of the water masers in the CSE around PZ Cas. This is the first time to monitor the water masers of this source over two years. As already reported for another RSG, S per (Asaki et al., 2010), the water maser distribution of PZ Cas has been very stable so that we could identify multiple maser spots in the monitoring program.

For the precise astrometry, we have developed the new phase calibration method called Direct Phase Transfer (DPT) method. This method works well in especially for the case that the signal-to-noise ratio is too small to obtain the reliable phase calibration solution with the conventional analysis method using AIPS software. Using this method, we could obtain the maser positions of PZ Cas with the typical positional accuracy of 93 and 110 μas eastward and northward, respectively. The annual parallax to PZ Cas was determined to be 0.356 $\pm$ 0.026 mas, corresponding to 2.81 $^{+0.22}_{-0.19}$ kpc. We re-scaled the previously obtained luminosity values with our trigonometric parallax to derive the mass and age of PZ Cas. Using the effective temperature of 3600 K (Levesque et al., 2005), we estimated the initial mass and the lifetime of PZ Cas to be $\sim$ 25 $M_\odot$ and $\sim$ 8 Myr, respectively, by comparison with the H-R diagram and evolutionary tracks calculated for massive stars (Meynet & Maeder, 2003).

By using the model fitting of the water maser proper motions to the radially expanding CSE, we could derive the systemic proper motion, that is, the stellar proper motion, to be $(\mu^*_\alpha \cos\delta,\ \mu^*_\delta)$ = (–3.7 $\pm$ 0.2, –2.0 $\pm$ 0.3) mas yr^{-1} eastward and northward, respectively. We calculated the peculiar motion of PZ Cas using the obtained annual parallax, stellar

proper motion, and stellar radial velocity. The resultant peculiar motion is $(U_s, V_s, W_s) = (22.8 \pm 4.4, 7.1 \pm 2.2, -5.7 \pm 4.0)$ km s^{-1}. We therefore found a large peculiar motion in PZ Cas as already observed for the Galactic HMSFRs (Reid et al., 2009b). We discussed about the origin of the large peculiar motion of PZ Cas by examining the three hypothesis of (1) runaway star hypothesis, (2) supershell hypothesis, and (3) epicyclic motion hypothesis in the Milky Way. By comparing PZ Cas's peculiar motion with the velocities of the other member stars belonging to the Cas OB5 association, we rejected the runaway star hypothesis. Therefore, the origin of PZ Cas's peculiar motion can be attributed to that of Cas OB5.

We then compared the peculiar motions of the Cas OB5 member to those of and Cas OB4 to examine the supershell hypothesis. In the case of the comparison of each of the peculiar motions of the member stars of the two OB associations, we cannot see a clear evidence of the expanding motion due to the large supershell. On the other hand, if we compare the averaged peculiar motions between the two OB associations, there may be an expanding motion from an originating point with a zero peculiar motion. We have to note that the velocity dispersions of the OB associations are very large, and that there is not enough energy sources to form the supershell.

The epicyclic motion hypothesis in galaxy dynamics is an attractive idea to explain the peculiar motions not only for PZ Cas or Cas OB5, but also HMSFRs whose 3-D motions have been measured with the VLBI astrometry. Recent large N-body hydrodynamical simulations have shown that non-stationary spiral arms can be formed in a disk galaxy without of the density wave (Baba et al., 2009). According to the simulation results, young objects in the disk have random large peculiar motions because of the epicyclic motions as large as what the VLBI astrometric observations have shown. At this moment, although we have no concrete evidence to select between the latter two hypothesis as the origin of the peculiar motion of PZ Cas, the epicyclic motion hypothesis is plausible because we cannot find enough energy to form the supershell.

In this thesis study to compare the proper motions of the OB associations, we recognized that the number of RSGs radiating the astronomical masers are quite small. Therefore we cannot obtain enough samples to discuss about the origin of the large peculiar motions. On the other hand, accuracies of the annual parallaxes and proper motions provided by *Hipparcos* are not enough to investigate above hypotheses. *GAIA* satellite was launched in December 2012 for the next-generation precise astrometry project. *Nano-JASMINE*, a Japanese space astrometry project, will be launched soon to observe in the infrared region. We expect that these projects will provide a large amount of high quality astrometric data to investigate the origin of the peculiar motions, which has been recognized by pioneering works with VLBI astrometry.

Acknowledgement

I would like to acknowledge Dr. Yasuhiro Murata, Dr. Yoshiharu Asaki, Dr. Hiroshi Imai, Dr. Tomoaki Oyama, Dr. Katsunori Shibata, and Mr. Takafumi Haga for very useful comments and suggestions. I have been supported by scholarly studies grants from the VERA archive data. This work made use of the VERA/Mizusawa VLBI observatory is a branch of the National Astronomical Observatory of Japan, National Institutes of Nature Sciences. The authors acknowledge the use of NASA's SkyView facility (http://skyview.gsfc.nasa.gov) located at NASA Goddard Space Flight Center. I was financially supported by the Center for the Promotion of Integrated Science of the Graduate University of Advanced Studies for this publication.

Bibliography

Abt, H. A, Levy, S. G., & Gandet, T. L. 1972, ApJ, 77, 128

Ando, K., Nagayama, T., Omodaka, T., et al. 2011, PASJ, 63, 45

Asaki, Y., Sudou, H., Kono, Y., et al. 2007, PASJ, 59, 397

Asaki, Y., Deguchi, S., Imai, H., et al. 2010, ApJ, 721, 267

Asaki, Y., Imai, H., Sobolev, A. M., & Parfenov, S. Y. 2014, ApJ, 787, 54

Baba, J., Asaki, Y., Makino, J., et al. 2009, ApJ, 706, 471

Bartel, N., Herring, T. A., Ratner, M. I., Shapiro, I. I., & Corey, B. E. 1986, `Nature`, 319, 733

Bartkiewicz, A., Brunthaler, A., Szymczak, M., van Langevelde, H. J., & Reid, M. J. 2008, A&A, 490, 787

Battrick, B. 1989, ESA SP, Paris: European Space Agency, 1989, edited by Battrick, Bruce,

Blaauw, A. 1961, BAIN, 15, 265

Blaha, C., & Humphreys, R. M. 1989, AJ, 98, 1598

Brunthaler, A., Reid, M. J., Menten, K. M., et al. 2009, ApJ, 693, 424

Burton, W. B., & Bania, T. M. 1974, A&A, 33, 425

Chen, X., Shen, Z-Q., Imai, H., & Kamohara, R. 2006, ApJ, 640, 982

Choi, Y. K., Hirota, T.,Honma, M., et al. 2008, PASJ, 60, 1007

Dame, T. M., Hartmann, Dap., & Thaddeus, P. 2001, ApJ, 547, 792

Deguchi, S. 1977, PASJ, 29, 669

Dehnen, W., & Binney, J. J. 1998, MNRAS, 298, 387

Dickinson, D. F., & Chaisson, E. J. 1973, ApJL, 181, L135

Dickinson, D. F. 1976, ApJS, 30, 259

Elitzur, M. 1992, ARAA, 30, 75

Engels, D., Schmid-Burgk, J., & Walmsley, C. M. 1986, A&A, 167, 129

Evans, D. S. 1967, IAUS, 30, 57

Famaey, B., Jorissen, A., Luri, X., et al. 2005, A&A, 430, 165

Fehrenbach, Ch., Duflot, M., Genty, V., & Amieux, G., 1996, BICDS, 48, 11

Fich, M. 1986, ApJ, 303, 465

Fujii, M. S., & Zwart, S. P. 2011, Science, 334, 1380

Garmany, C. D., & Stencel, R. E. 1992, A&AS, 94, 211

Genzel, R., Reid, M. J., Moran, J. M., & Downes, D. 1981, ApJ, 244, 884

Georgelin, Y. M., & Georgelin, Y. P. 1976, A&A, 49, 57

Gómez, G. C. 2006, AJ, 132, 2376

Gundermann, E. J. 1965, Ph.D. Thesis, Harvard Univ., Cambrige, Mass.

Gupta, A. C., Subramaniam, A., Sagar, R., & Griffiths, W. K. 2000, A&AS, 145, 365

Hachisuka, K., Brunthaler, A., Menten, K. M., et al. 2006, ApJ, 645, 337

Hada, K., Doi, A., Kino, M., et al. 2011, `Nature`, 477, 185

Hirota, T., Bushimata, T., Choi, Y. K., et al. 2007, PASJ, 59, 897

Høg, E., Fabricius, C., Makarov, V. V., et al. 2000, A&A, 355, L27

Honma, M., Fujii, T., Hirota, T., et al. 2003, PASJ, 55, L57

Honma, M., Bushimata, T., Choi, Y. K., et al. 2007, PASJ, 59, 889

Honma, M., Kijima, M., Suda, H., et al. 2008, PASJ, 60, 935

Honma, M., Hirota, T., Jike, T., et al. 2010, PNAOJ, 13, 57

Honma, M., Nagayama, T., Ando, K., et al. 2012, PASJ, 64, 136

Humphreys, R. M. 1970, ApJ, 160, 1149

Humphreys, R. M. 1978, ApJS, 38, 309

Humphreys, R. M. 1986, Luminous Stars and Associations in Galaxies, 116, 45

Imai, H., Omi, R., Kurayama, T., et al. 2011, PASJ, 63, 1293

Johnson, D. R. H., & Soderblom, D. R. 1987, AJ, 93, 864

Josselin, E., Blommaert, J. A. D. L., Groenewegen, M. A. T., Omont, A., & Li, F. L. 2000, A&A, 357, 225

Kamohara, R., Deguchi, S., Miyoshi, M., & Shen, Z-Q. 2005, PASJ, 57, 341

Kerr, F. J., & Lynden-Bell, D. 1986, MNRAS, 221, 1023

Kharchenko, N. V., Piskunov, A. E., Röser, S., & Scholz, R. D. 2005, A&A, 438, 1163

Kraft, R. P. 1958, ApJ, 128, 161

Lee, H.-T., & Lim, J. 2008, ApJ, 679, 1352

Levesque, E. M., Massey, P., Olesn, K. A. G., et al. 2005, ApJ, 628, 973

Lin, C. C., & Shu, F. H. 1964, ApJ, 140, 646

Liszt, H. S., & Burton, W. B. 1981, ApJ, 243, 778

Litvak, M. M., McWorter, A. L., Meeks, M. L., Zeiger, H. J. 1966, *Phys. Rev. Lett.* 17, 821

Mauron, N., & Josselin, E. 2011, A&A, 526, A156

Massey, P. 2003, ARAA, 41, 15

Mel'Nik, A. M., Dambis, A. K., & Rastorguev, A. S. 2001, Astronomy Letters, 27, 521

Mel'nik, A. M., & Dambis, A. K. 2009, MNRAS, 400, 518

Menten, K. M., Reid, M. J., Forbrich, J., & Brunthaler, A. 2007, A&A, 474, 515

Mermilliod, J. C., Mayor, M., & Udry, M. 2008, A&A, 485, 303

Meynet, G., & Maeder, A. 2003, A&A, 404, 975

Moór, A., & Kiss, C. 2003, Commmunications of the Konkoly Observatory Hungary, 103, 149

Moscadelli, L., Reid, M. J., Menten, K. M., et al. 2009, ApJ, 693, 406

Münch, G. 1957, ApJ, 125, 42

Nagayama, T., Takeda, K., Omodaka, T., et al. 2008, PASJ, 60, 1069

Nakanishi, H., & Sofue, Y. 2006, PASJ, 58, 847

Petrov, L., Hirota, T., Honma, M., et al. 2007, AJ, 133, 2487

Perkins, F., Gold, T., & Salpeter, E. E. 1966, ApJ, 145, 361

Perryman, M. A. C., Lindegren, L., Kovalevsky, J., et al. 1997, A&A, 323, L49

Reid, M. J., & Moran, J. M. 1981, ARAA, 19, 231

Reid, M. J., Menten, K. M., Brunthaler, A., et al. 2009, ApJ, 693, 397

Reid, M. J., Menten, K. M., Zheng, X. W., et al. 2009, ApJ, 700, 137

Reid, M. J., & Honma, M. 2013, arXiv:1312.2871

Richards, A. M. S., Elitzur, M., & Yates, J. A. 2011, A&A, 525, A56

Richards, A. M. S., Etoka, S., Gray, M. D., et al. 2012, A&A, 546, A16

Rioja, M., Dodson, R., Asaki, Y., Hartnett, J., & Tingay, S. 2012, AJ, 144, 121

Russeil, D. 2003, A&A, 397, 133

Sakai, N., Honma, M., Nakanishi, H., et al. 2012, PASJ, 64, 108

Sakai, N., Sato, M., Motogi, K., et al. 2013, arXiv:1308.3004

Sanna, A., Reid, M. J., Moscadelli, L., et al. 2009, ApJ, 706, 464

Sato, M., Hirota, T., Honma, M., et al. 2008, PASJ, 60, 975

Schilbach, E., Röumlser, S. 2008, A&A, 489, 105

Schönrich, R., Binney, J., & Dehnen, W. 2010, MNRAS, 403, 1829

Shintani, M., Imai, H., Ando, K., et al. 2008, PASJ, 60, 1077

Toomre, A. 1981, Structure and Evolution of Normal Galaxies, 111

Valdes, F., Gupta, R., Rose, J. A., Singh, H. P., & Bell, D. J. 2004, ApJS, 152, 251

van Leeuwen F. 2007, A&A, 474, 653

Wada, K., Baba, J., & Saitoh, T. R. 2011, ApJ, 735, 1

Weaver, H., Williams, D. R. W., Dieter, N. H., & Lum, W. T. 1965, `Nature`, 208, 29

Wilson, R. E. 1953, General Catalogue of Stellar Radial Velocities (Washington, DC: Carnegie Institute of Washington)

Xu, Y., Reid, M. J., Zheng, X. W., & Menten, K. M. 2006, Science, 311, 54

Xu, Y., Reid, M. J., Menten, K. M., et al. 2009, ApJ, 693, 413

Zhang, B., Zheng, X. W., Reid, M. J., et al. 2009, ApJ, 693, 419

Zhang, B., Reid, M. J., Menten, K. M., & Zheng, X. W. 2012, ApJ, 744, 23

Zhang, B., Reid, M. J., Menten, K. M., Zheng, X. W. & Brunthaler, A. 2012, A&A, 544, A42

Appendix A

Detected Maser Spots

Below are the tables of maser spots obtained by the phase referencing analysis and used for determining proper motions. These spots of observations of 12 epoch (A to L epoch) obtained from the data analysis techniques described in Chapter 2. Detected maser spots are listed in this appendix with their flux densities, positions, and positional errors. The table are prepared for each of the epochs ad listed Table 2.1.

Table A.1: H_2O maser spots table of PZ Cas at epoch A

V_{LSR} [km s^{-1}]	Flux [Jy]	$\Delta\alpha_A$ [mas]	$\Delta\delta_A$ [mas]	ϵ_α [mas]	ϵ_δ [mas]
-40.525	0.585	-0.987	53.488	0.196	0.191
-40.736	0.970	0.391	51.242	0.130	0.117
-40.736	1.182	-0.782	53.890	0.114	0.098
-40.736	0.650	66.209	-43.262	0.177	0.170
-40.946	0.938	0.227	51.098	0.138	0.126
-40.946	2.305	-0.685	53.917	0.087	0.060
-40.946	1.034	65.914	-42.768	0.129	0.115
-41.157	0.607	0.071	51.042	0.197	0.192
-41.157	2.583	-0.640	54.092	0.084	0.055
-41.157	1.388	0.605	57.607	0.108	0.089
-41.157	1.045	65.994	-42.789	0.128	0.115
-41.368	1.708	-0.554	54.083	0.101	0.081
-41.368	5.470	0.639	57.664	0.075	0.040
-41.368	0.715	65.930	-42.673	0.185	0.179
-41.579	14.876	0.650	57.672	0.073	0.035
-41.789	17.119	0.680	57.651	0.073	0.035
-42.000	10.347	0.661	57.666	0.074	0.036
-42.211	4.361	0.715	57.746	0.077	0.043
-42.211	1.198	1.226	60.006	0.119	0.104
-42.421	1.836	1.217	58.504	0.091	0.067
-42.421	1.208	1.167	59.574	0.112	0.094
-42.632	0.708	0.948	58.069	0.171	0.164

Table A.2: H_2O maser spots table of PZ Cas at epoch B

V_{LSR} [km s^{-1}]	Flux [Jy]	$\Delta\alpha_A$ [mas]	$\Delta\delta_A$ [mas]	ϵ_α [mas]	ϵ_δ [mas]
-40.736	0.721	-0.117	51.365	0.209	0.199
-40.736	0.872	-1.557	53.773	0.177	0.166
-40.946	1.015	-0.348	51.211	0.165	0.153
-40.946	1.841	-1.386	53.893	0.109	0.089
-41.157	1.513	-0.433	51.171	0.124	0.107
-41.157	2.082	-1.336	54.186	0.103	0.081
-41.368	1.453	-1.176	54.007	0.128	0.112
-41.368	2.823	-0.017	57.789	0.090	0.064
-41.579	9.493	-0.013	57.809	0.075	0.039
-41.789	13.646	-0.004	57.811	0.074	0.037
-42.000	9.186	-0.004	57.834	0.075	0.039
-42.211	4.419	0.023	57.825	0.081	0.049
-42.421	1.654	0.589	58.590	0.117	0.099
-42.421	1.007	0.414	60.472	0.168	0.156
-42.632	0.703	0.490	58.632	0.218	0.209
-42.632	0.819	0.750	60.349	0.191	0.180
-51.271	0.824	-17.601	-13.598	0.187	0.177
-51.481	1.691	-17.688	-13.621	0.114	0.094
-51.692	2.079	-17.701	-13.549	0.100	0.078
-51.903	1.647	-17.746	-13.530	0.114	0.094

Table A.3: H_2O maser spots table of PZ Cas at epoch C

V_{LSR} [km s^{-1}]	Flux [Jy]	$\Delta\alpha_A$ [mas]	$\Delta\delta_A$ [mas]	ϵ_α [mas]	ϵ_δ [mas]
-40.736	1.367	-0.704	51.593	0.129	0.119
-40.736	1.677	-1.947	53.640	0.113	0.099
-40.736	0.649	65.247	-43.312	0.237	0.243
-40.946	1.751	-0.875	51.008	0.111	0.096
-40.946	3.090	-1.878	53.890	0.086	0.061
-40.946	1.192	65.320	-43.244	0.143	0.136
-41.157	2.377	-0.896	50.884	0.096	0.075
-41.157	3.635	-1.785	54.069	0.083	0.055
-41.157	0.833	-0.484	57.779	0.194	0.194
-41.157	1.379	65.206	-43.133	0.130	0.120
-41.368	1.557	-0.936	50.810	0.119	0.106
-41.368	2.091	-1.707	54.204	0.101	0.082
-41.368	3.769	-0.497	57.742	0.082	0.053
-41.368	0.880	65.260	-43.139	0.182	0.181
-41.579	13.330	-0.483	57.720	0.073	0.036
-41.789	20.104	-0.485	57.718	0.073	0.036
-42.000	14.933	-0.498	57.712	0.073	0.036
-42.211	7.222	-0.461	57.693	0.076	0.041
-42.211	1.792	-0.042	60.552	0.119	0.106
-42.421	2.993	0.080	58.473	0.087	0.062
-42.421	1.471	0.012	60.321	0.123	0.111
-42.632	1.261	0.096	58.439	0.131	0.121
-42.632	0.786	0.048	60.251	0.189	0.189
-43.054	1.032	-0.849	63.353	0.153	0.147
-43.264	0.796	-0.643	62.943	0.188	0.188
-51.271	0.824	-18.257	-13.661	0.182	0.181
-51.481	1.226	-18.207	-13.807	0.133	0.123
-51.692	1.568	-18.150	-13.809	0.116	0.102
-51.903	1.024	-18.213	-13.736	0.151	0.145

Table A.4: H_2O maser spots table of PZ Cas at epoch D

V_{LSR} [km s^{-1}]	Flux [Jy]	$\Delta\alpha_A$ [mas]	$\Delta\delta_A$ [mas]	ϵ_α [mas]	ϵ_δ [mas]
-40.525	0.408	-1.573	51.006	0.208	0.210
-40.525	0.739	-3.057	53.229	0.130	0.119
-40.736	0.997	-1.721	50.755	0.111	0.095
-40.736	2.013	-2.934	53.331	0.083	0.055
-40.736	1.004	64.639	-44.037	0.110	0.094
-40.946	1.676	-1.862	50.501	0.089	0.064
-40.946	3.862	-2.880	53.405	0.075	0.041
-40.946	1.920	64.568	-43.865	0.085	0.059
-41.157	2.094	-1.908	50.487	0.083	0.055
-41.157	3.974	-2.813	53.573	0.075	0.040
-41.157	0.715	-1.504	57.354	0.142	0.134
-41.157	2.014	64.482	-43.801	0.084	0.057
-41.368	1.483	-1.857	50.387	0.094	0.072
-41.368	2.862	-2.654	53.737	0.078	0.047
-41.368	3.040	-1.481	57.303	0.078	0.045
-41.368	1.328	64.423	-43.761	0.098	0.078
-41.368	0.605	63.738	-42.274	0.163	0.159
-41.579	1.425	-2.453	53.890	0.106	0.089
-41.579	11.503	-1.454	57.305	0.073	0.035
-41.579	0.549	64.369	-43.705	0.215	0.217
-41.579	0.577	63.597	-41.980	0.206	0.207
-41.789	21.950	-1.461	57.306	0.072	0.034
-42.000	20.016	-1.459	57.310	0.072	0.034
-42.000	0.481	-31.491	-65.982	0.320	0.332
-42.211	9.963	-1.462	57.341	0.073	0.035
-42.211	1.927	-0.927	59.996	0.090	0.067
-42.211	0.536	-31.501	-66.066	0.208	0.210
-42.421	3.958	-0.906	58.012	0.076	0.042
-42.421	1.970	-0.884	59.946	0.087	0.062
-42.632	1.851	-0.977	57.990	0.085	0.058
-42.632	1.019	-0.890	59.774	0.108	0.092
-42.843	0.840	-1.765	62.523	0.122	0.109
-43.054	0.959	-1.756	62.587	0.111	0.095
-43.264	0.836	-1.778	62.571	0.118	0.105
-48.321	0.352	0.413	78.422	0.239	0.244
-48.532	0.634	0.604	78.394	0.144	0.137

Table A.5: H_2O maser spots table of PZ Cas at epoch E

V_{LSR} [km s^{-1}]	Flux [Jy]	$\Delta\alpha_A$ [mas]	$\Delta\delta_A$ [mas]	ϵ_α [mas]	ϵ_δ [mas]
-40.525	0.676	-2.239	50.675	0.166	0.166
-40.525	0.851	-3.640	52.778	0.139	0.133
-40.525	0.655	64.309	-44.555	0.170	0.171
-40.736	1.093	-2.305	50.532	0.120	0.110
-40.736	2.775	-3.531	52.926	0.081	0.053
-40.736	1.381	64.198	-44.451	0.105	0.089
-40.946	1.518	-2.440	50.305	0.103	0.087
-40.946	4.942	-3.498	53.054	0.076	0.041
-40.946	2.366	64.173	-44.418	0.086	0.061
-41.157	1.873	-2.529	50.093	0.093	0.073
-41.157	4.670	-3.435	53.155	0.076	0.042
-41.157	0.692	-2.107	57.101	0.176	0.178
-41.157	2.167	64.164	-44.333	0.088	0.065
-41.368	1.117	-2.481	50.119	0.116	0.105
-41.368	2.616	-3.265	53.343	0.082	0.054
-41.368	2.566	-2.046	57.063	0.082	0.054
-41.368	1.329	64.034	-44.377	0.105	0.090
-41.368	0.595	63.338	-42.752	0.185	0.189
-41.579	1.082	-3.100	52.831	0.140	0.136
-41.579	10.608	-2.046	56.994	0.073	0.036
-41.579	0.553	-2.844	2.072	0.247	0.259
-41.789	21.338	-2.059	56.981	0.072	0.034
-42.000	20.962	-2.057	57.008	0.073	0.034
-42.211	11.806	-2.018	57.089	0.073	0.036
-42.211	1.579	-1.591	59.857	0.124	0.115
-42.421	5.220	-1.737	57.411	0.076	0.041
-42.421	1.762	-1.478	59.459	0.099	0.081
-42.632	1.910	-1.671	57.591	0.091	0.069
-42.632	1.071	-1.438	59.407	0.122	0.113
-42.843	0.954	-2.333	62.171	0.128	0.120
-43.054	1.263	-2.296	62.263	0.110	0.097
-43.264	1.169	-2.409	62.206	0.112	0.099
-48.321	0.539	0.039	77.784	0.201	0.207
-48.532	0.611	-0.052	78.223	0.181	0.184

Table A.6: H_2O maser spots table of PZ Cas at epoch F

V_{LSR} [km s^{-1}]	Flux [Jy]	$\Delta\alpha_A$ [mas]	$\Delta\delta_A$ [mas]	ϵ_α [mas]	ϵ_δ [mas]
-40.525	0.369	-3.029	49.938	0.223	0.218
-40.525	0.572	-4.379	52.061	0.154	0.143
-40.525	0.671	63.901	-45.764	0.136	0.123
-40.736	0.520	-3.001	49.901	0.165	0.155
-40.736	1.757	-4.291	52.086	0.084	0.056
-40.736	1.692	63.904	-45.714	0.085	0.057
-40.946	0.538	-3.150	49.422	0.167	0.158
-40.946	3.494	-4.224	52.154	0.076	0.041
-40.946	3.175	63.803	-45.611	0.076	0.042
-41.157	0.584	-3.243	49.394	0.161	0.151
-41.157	3.127	-4.197	52.253	0.077	0.043
-41.157	0.574	-2.803	56.255	0.163	0.154
-41.157	3.412	63.774	-45.543	0.076	0.042
-41.368	0.452	-3.313	49.413	0.196	0.189
-41.368	1.879	-4.001	52.804	0.084	0.056
-41.368	1.697	-2.761	56.263	0.087	0.059
-41.368	2.248	63.719	-45.515	0.081	0.050
-41.368	0.720	62.931	-43.800	0.135	0.121
-41.368	0.465	-3.543	1.286	0.191	0.183
-41.579	0.914	-3.839	52.725	0.125	0.109
-41.579	6.595	-2.802	56.211	0.073	0.036
-41.579	1.025	63.740	-45.544	0.116	0.098
-41.579	0.788	62.986	-43.730	0.138	0.125
-41.579	0.556	-3.676	1.351	0.182	0.174
-41.789	14.156	-2.812	56.225	0.072	0.034
-42.000	15.959	-2.830	56.221	0.072	0.034
-42.211	9.773	-2.823	56.285	0.073	0.035
-42.211	1.292	-2.249	58.614	0.110	0.091
-42.211	0.558	-32.907	-67.861	0.206	0.200
-42.421	3.916	-2.648	56.565	0.075	0.040
-42.421	1.384	-2.188	58.544	0.095	0.071
-42.421	0.312	-33.007	-67.499	0.282	0.280
-42.632	1.308	-2.359	56.771	0.095	0.071
-42.632	0.829	-2.125	58.402	0.121	0.105
-42.843	0.890	-3.020	61.334	0.115	0.097
-43.054	1.235	-3.114	61.398	0.096	0.073
-43.264	0.938	-3.063	61.346	0.110	0.091

Table A.7: H_2O maser spots table of PZ Cas at epoch G

V_{LSR} [km s^{-1}]	Flux [Jy]	$\Delta\alpha_A$ [mas]	$\Delta\delta_A$ [mas]	ϵ_α [mas]	ϵ_δ [mas]
-40.525	0.341	-4.761	52.050	0.226	0.202
-40.525	0.467	63.743	-45.877	0.172	0.149
-40.736	1.107	-4.652	52.035	0.102	0.075
-40.736	1.182	63.649	-45.873	0.099	0.071
-40.946	2.176	-4.611	52.030	0.082	0.050
-40.946	2.308	63.638	-45.859	0.081	0.048
-41.157	2.075	-4.533	52.150	0.084	0.052
-41.157	0.476	-3.225	56.138	0.199	0.175
-41.157	2.665	63.516	-45.760	0.079	0.045
-41.157	0.539	-3.996	1.155	0.179	0.156
-41.368	1.362	-4.351	52.538	0.093	0.064
-41.368	1.398	-3.120	56.101	0.092	0.063
-41.368	2.088	63.460	-45.712	0.082	0.049
-41.368	0.629	62.942	-44.353	0.147	0.123
-41.368	0.667	-4.005	1.045	0.141	0.117
-41.579	0.992	-4.300	52.664	0.122	0.097
-41.579	4.438	-3.167	56.171	0.075	0.039
-41.579	1.074	63.464	-45.685	0.116	0.091
-41.579	0.610	62.901	-44.051	0.176	0.152
-41.579	0.566	-3.837	0.973	0.187	0.164
-41.789	9.959	-3.166	56.159	0.073	0.036
-42.000	11.676	-3.166	56.176	0.073	0.036
-42.211	7.214	-3.165	56.261	0.075	0.038
-42.211	1.480	-2.612	58.924	0.125	0.100
-42.421	3.211	-2.943	56.636	0.078	0.043
-42.421	1.436	-2.580	58.638	0.099	0.071
-42.632	1.175	-2.845	56.706	0.097	0.069
-42.632	0.854	-2.484	58.580	0.115	0.089
-42.843	0.774	-3.338	61.203	0.119	0.094
-43.054	1.037	-3.430	61.240	0.102	0.075
-43.264	0.659	-3.491	61.282	0.130	0.106

Table A.8: H_2O maser spots table of PZ Cas at epoch H

V_{LSR} [km s^{-1}]	Flux [Jy]	$\Delta\alpha_A$ [mas]	$\Delta\delta_A$ [mas]	ϵ_α [mas]	ϵ_δ [mas]
-40.736	0.632	-5.519	52.102	0.235	0.214
-40.736	0.604	63.313	-45.955	0.245	0.223
-40.946	0.856	-5.316	52.161	0.180	0.159
-40.946	1.264	63.233	-45.894	0.135	0.113
-41.157	0.750	-5.173	52.452	0.209	0.188
-41.157	1.569	63.189	-45.915	0.121	0.098
-41.368	0.716	-4.969	52.970	0.215	0.194
-41.368	1.014	-3.730	56.559	0.162	0.141
-41.368	1.218	63.196	-45.968	0.141	0.120
-41.579	2.573	-3.852	56.426	0.098	0.071
-41.789	5.239	-3.856	56.422	0.085	0.055
-42.000	7.072	-3.865	56.477	0.083	0.052
-42.211	4.552	-3.840	56.530	0.087	0.057

Table A.9: H_2O maser spots table of PZ Cas at epoch I

V_{LSR} [km s^{-1}]	Flux [Jy]	$\Delta\alpha_A$ [mas]	$\Delta\delta_A$ [mas]	ϵ_α [mas]	ϵ_δ [mas]
-40.736	0.765	62.479	-46.073	0.201	0.167
-40.946	0.999	62.634	-46.181	0.171	0.134
-41.157	0.605	-6.401	51.579	0.248	0.215
-41.157	1.540	62.552	-46.107	0.135	0.092
-41.368	1.074	-4.668	56.466	0.162	0.124
-41.368	0.809	62.392	-46.112	0.195	0.161
-41.579	2.556	-4.791	56.452	0.116	0.066
-41.789	5.737	-4.807	56.477	0.105	0.048
-42.000	7.564	-4.833	56.521	0.105	0.047
-42.211	5.219	-4.778	56.639	0.107	0.050
-42.421	1.918	-4.641	56.718	0.123	0.077

Table A.10: H_2O maser spots table of PZ Cas at epoch J

V_{LSR} [km s^{-1}]	Flux [Jy]	$\Delta\alpha_A$ [mas]	$\Delta\delta_A$ [mas]	ϵ_α [mas]	ϵ_δ [mas]
-40.525	0.398	-7.259	51.673	0.267	0.227
-40.736	0.589	-7.241	51.368	0.191	0.159
-40.736	0.923	62.015	-46.785	0.134	0.104
-40.946	0.837	-7.356	51.365	0.145	0.115
-40.946	1.424	61.900	-46.871	0.103	0.073
-41.157	1.152	-6.983	52.337	0.117	0.087
-41.157	1.796	61.855	-46.727	0.093	0.062
-41.368	1.048	-6.840	52.443	0.128	0.098
-41.368	0.845	-5.628	55.959	0.149	0.119
-41.368	1.349	61.831	-46.761	0.109	0.079
-41.368	0.558	60.518	-44.531	0.211	0.177
-41.368	0.840	-6.570	0.567	0.150	0.120
-41.579	0.616	-6.686	52.470	0.197	0.164
-41.579	3.277	-5.648	56.052	0.080	0.045
-41.579	0.578	61.778	-46.669	0.208	0.174
-41.579	0.659	60.732	-44.674	0.186	0.153
-41.579	0.966	-6.571	0.558	0.137	0.107
-41.789	7.993	-5.661	56.062	0.074	0.036
-41.789	0.696	-6.500	0.538	0.208	0.174
-42.000	10.646	-5.681	56.104	0.074	0.035
-42.000	0.781	-35.904	-68.699	0.206	0.173
-42.211	8.418	-5.675	56.206	0.075	0.038
-42.211	1.396	-5.181	58.221	0.143	0.113
-42.211	0.956	-35.894	-68.673	0.194	0.161
-42.421	3.165	-5.609	56.303	0.081	0.046
-42.421	1.086	-5.117	58.135	0.128	0.098
-42.421	0.444	-35.907	-68.495	0.267	0.228
-42.632	0.923	-5.533	56.323	0.136	0.106
-42.632	0.590	-5.078	57.818	0.194	0.161
-42.843	0.813	-5.946	60.905	0.148	0.118
-43.054	1.002	-5.979	60.952	0.124	0.095
-43.264	0.587	-5.976	60.983	0.191	0.159

Table A.11: H_2O maser spots table of PZ Cas at epoch K

V_{LSR} [km s^{-1}]	Flux [Jy]	$\Delta\alpha_A$ [mas]	$\Delta\delta_A$ [mas]	ϵ_α [mas]	ϵ_δ [mas]
-40.736	0.329	-7.604	50.837	0.222	0.208
-40.736	0.703	61.852	-47.578	0.122	0.102
-40.946	0.591	-7.412	50.930	0.141	0.123
-40.946	1.613	61.761	-47.523	0.085	0.054
-41.157	0.827	-7.180	51.902	0.118	0.097
-41.157	0.374	-5.798	55.443	0.220	0.205
-41.157	1.899	61.752	-47.472	0.083	0.052
-41.157	0.421	-6.974	-0.008	0.198	0.183
-41.368	1.066	-7.164	52.075	0.100	0.075
-41.368	1.071	-5.941	55.453	0.100	0.075
-41.368	1.247	61.693	-47.401	0.093	0.067
-41.368	0.480	60.755	-45.351	0.171	0.154
-41.368	0.540	-6.883	0.039	0.155	0.138
-41.579	0.701	-7.041	52.206	0.134	0.115
-41.579	3.435	-5.960	55.513	0.076	0.040
-41.579	0.575	61.696	-47.535	0.156	0.139
-41.579	0.589	60.548	-45.235	0.153	0.136
-41.579	0.720	-6.907	-0.055	0.132	0.112
-41.789	8.191	-5.966	55.545	0.073	0.035
-41.789	0.607	-6.901	-0.063	0.177	0.161
-42.000	12.205	-5.981	55.598	0.073	0.034
-42.000	0.533	-36.283	-69.323	0.229	0.214
-42.211	9.764	-5.967	55.665	0.073	0.034
-42.211	1.621	-5.354	57.486	0.094	0.067
-42.211	0.592	-36.203	-69.349	0.180	0.164
-42.421	4.260	-5.916	55.742	0.074	0.038
-42.421	1.663	-5.319	57.438	0.086	0.057
-42.421	0.433	-36.422	-69.476	0.196	0.181
-42.632	1.139	-5.836	55.760	0.095	0.069
-42.632	0.855	-5.354	57.330	0.110	0.087
-42.843	0.881	-6.259	60.408	0.108	0.085
-43.054	1.169	-6.291	60.421	0.094	0.067
-43.264	0.676	-6.253	60.322	0.127	0.108

Table A.12: H_2O maser spots table of PZ Cas at epoch L

V_{LSR} [km s^{-1}]	Flux [Jy]	$\Delta\alpha_A$ [mas]	$\Delta\delta_A$ [mas]	ϵ_α [mas]	ϵ_δ [mas]
-40.525	0.324	61.982	-48.891	0.207	0.187
-40.736	0.328	-8.496	50.226	0.204	0.184
-40.736	0.418	61.733	-48.836	0.167	0.146
-40.946	0.524	-8.422	50.354	0.141	0.119
-40.946	0.899	61.561	-48.655	0.101	0.074
-41.157	0.895	-7.998	51.305	0.105	0.080
-41.157	0.336	-6.719	54.665	0.217	0.196
-41.157	1.118	61.430	-48.591	0.095	0.067
-41.368	1.362	-7.948	51.473	0.088	0.058
-41.368	1.022	-6.768	54.866	0.099	0.072
-41.368	0.875	61.306	-48.500	0.107	0.082
-41.368	0.451	60.120	-46.290	0.170	0.149
-41.579	1.294	-7.884	51.639	0.091	0.062
-41.579	3.453	-6.805	54.873	0.075	0.039
-41.579	0.433	61.273	-48.535	0.182	0.161
-41.579	0.486	60.173	-46.360	0.165	0.145
-41.789	7.745	-6.785	54.933	0.073	0.035
-42.000	12.044	-6.823	55.021	0.073	0.034
-42.211	11.326	-6.828	55.124	0.073	0.034
-42.211	2.833	-6.257	56.316	0.082	0.049
-42.421	5.440	-6.793	55.191	0.074	0.036
-42.421	2.723	-6.208	56.373	0.078	0.044
-42.632	1.679	-6.746	55.199	0.083	0.050
-42.632	1.338	-6.239	56.221	0.088	0.058
-42.843	1.190	-7.196	59.743	0.091	0.062
-43.054	1.267	-7.177	59.789	0.088	0.059
-43.264	0.653	-7.171	59.699	0.122	0.099